water

MDPI

Article

Turbidity Currents Carrying Shallow Heat Invading Stable Deep-Water Areas May Be an Unrecognized Source of "Pollution" in the Ocean

Hao Tian [1,2], Guohui Xu [3,*], Jingtao Zhao [1,2,*], Yupeng Ren [4] and Hanru Wu [3]

[1] Qingdao Institute of Marine Geology, China Geological Survey, Qingdao 266237, China; tianhao199207@163.com
[2] Laboratory for Marine Mineral Resources, Qingdao Marine Science and Technology Center, Qingdao 266237, China
[3] Key Laboratory of Marine Environmental Geological Engineering, Ocean University of China, Qingdao 266100, China; wuhr0825@126.com
[4] Qingdao National Laboratory of Marine Science and Technology, Qingdao 266061, China; renyupeng@ouc.edu.cn
* Correspondence: xuguohui@ouc.edu.cn (G.X.); zhaojingtao113@163.com (J.Z.)

Abstract: When turbidity currents carrying shallow heat enter stable stratified lakes or oceans, they can trigger changes in temperature, dissolved chemicals, oxygen concentrations, and nutrient mixing through the stable stratified environmental water. Although it is common for warm turbidity currents to invade stable regions, the impact of turbidity current characteristics on environmental entrainment and the impact of temperature changes caused by the mixing of warm turbidity currents with the environment remains poorly understood. In this study, systematic experiments on warm turbidity currents were conducted to understand how sediment-driven turbidity currents lead to mixing in stable stratification using existing environmental entrainment numbers. The experimental results show that the dimensionless numbers R_s (the ratio of the change in environmental water concentration caused by salinity to sediment load), R_T (the ratio of the change in environmental water concentration caused by temperature difference to sediment load), and R_0 (non-dimensional density ratio) control the flow process of warm turbid plumes, and corresponding functional relationships are summarized. The frequent occurrence of warm turbidity currents events caused by increasingly prominent environmental problems cannot be ignored, as it directly affects the deep-water environment of lakes or coastal oceans, which may be an important contribution to heat transfer that has not been evaluated in previous ocean events.

Keywords: turbidity current; carrying heat; temperature structure; environmental entrainment; marine environment

Citation: Tian, H.; Xu, G.; Zhao, J.; Ren, Y.; Wu, H. Turbidity Currents Carrying Shallow Heat Invading Stable Deep-Water Areas May Be an Unrecognized Source of "Pollution" in the Ocean. *Water* **2024**, *16*, 3521. https://doi.org/10.3390/w16233521

Academic Editor: Alessandro Bergamasco

Received: 16 October 2024
Revised: 14 November 2024
Accepted: 3 December 2024
Published: 6 December 2024

1. Introduction

Turbidity currents are sediment-rich gravity currents that tend to be generated in relatively shallow, warm shelf environments, moving down slopes and spreading into deep-water lakes or deep oceans [1–5], as shown in Figure 1. The intrusion of external heat that breaks the stable and persistent energy stratification of pristine lakes or oceans is often referred to as "thermal pollution", and the steady state of lakes and coastal oceans is greatly affected by them. They will destabilize the stratification of heat, oxygen concentration, nutrients, and dissolved chemicals in the ambient water column, directly affecting the abundance and community structure of organisms in the marine environment [6–10]. In addition, the stable deep-sea environment makes deep-sea organisms highly sensitive to small temperature changes. Nematodes are a major component of marine sediments, accounting for more than 90% of the abundance of all benthic organisms in the deep sea [11,12]. Small species such as nematodes, which typically reproduce between days and months [13],

respond strongly and rapidly to changes in temperature. The relationship between the magnitude of temperature changes and changes in species richness provides evidence that small temperature changes of 0.1 C or less are sufficient to cause significant changes in the biodiversity and community structure of deep-sea nematode assemblages [14]. Therefore, whether turbidity currents from the shallower and warmer parts of the continental shelf have a "thermal pollution" effect during their migration from the seabed to deeper waters, thus affecting the temperature of the ambient water column, has not previously been considered in the field of global heat transport systems.

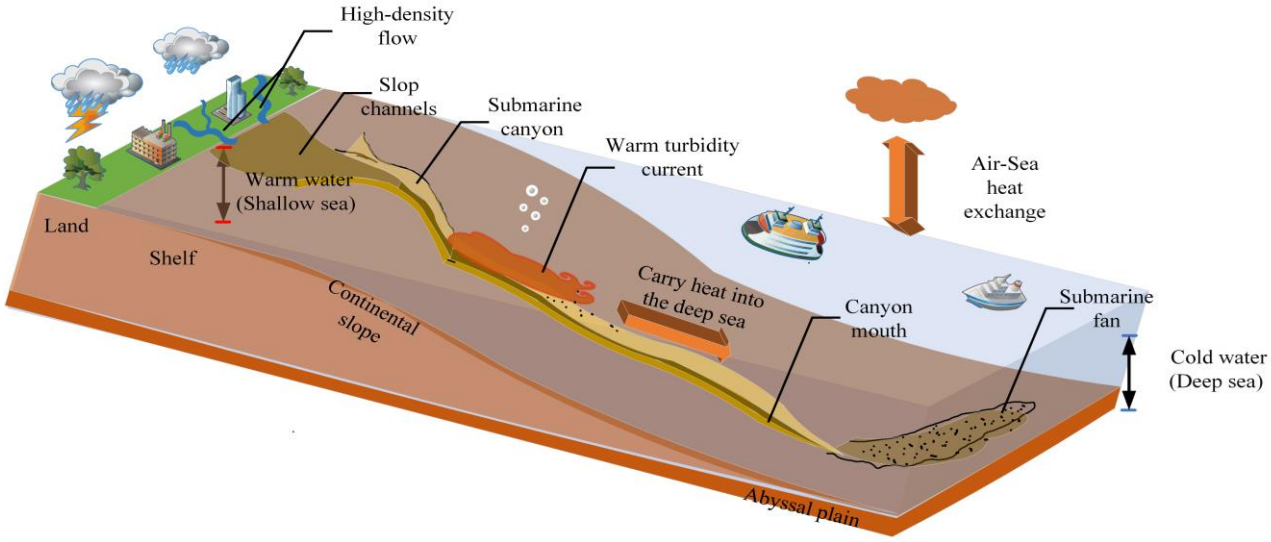

Figure 1. A schematic of the energy and matter changes affected by turbidity current transmission into ocean systems. (Note: Different triggers cause turbidity currents to enter the deep ocean environment along the ocean floor and carry heat from upper source areas further from the continental shelf into the deep ocean domain. Turbidity currents can act as a mechanism for transporting upper-layer heat, thus producing processes that alter the energy and material of the ocean system).

For high-density rivers flowing into the ocean, turbidity currents transport most of the sediment that is transported from the continental shelf or shallow delta environments to the deep-sea plain [15,16]. Sediments that move during these events are typically suspended not in cold, salty water that is characteristic of ocean basins but in fresher or warmer surface sea water or river water that has a lower density. The fate of the suspended sediment depends on the initial volume density of the turbidity current [17–19]. The volume density of the turbidity current depends on the initial density of river water (caused by the initial freshness caused by temperature) and sediment concentration (salinity that can be dissolved in water and concentration of undissolved sediment). The potential density of the ocean depends on the salinity, temperature, and depth of the sea water: the typical density of sea water is about $\rho_a \approx 1031$ kg/m^3 at a depth of 1 km and $\rho_a \approx 1040$ kg/m^3 at a depth of 2 km [20]. Due to the stable stratification of density, energy (heat), oxygen concentration, nutrients, and dissolved chemicals in the ocean, the warm turbidity currents generated in the continental shelf environment entering the deep sea are likely to contain light environmental water bodies and shallow heat, which may break the stable stratification of environmental water bodies along the turbidity current movement path. Table 1 summarizes the mean water temperature in the turbidity trigger areas and the ambient water temperature of the deeper seabed of the turbidity current path under different trigger conditions, indicating that there is a clear temperature difference between the ambient water temperature in the turbidity source areas and the migration areas. Most lakes and oceans exhibit significant density stratification or material stratification for most of the year, and it is important to understand the process of turbidity currents carrying heat and how to change this stratification.

Table 1. A comparison of ambient water temperature in the trigger source area and along the movement of turbidity currents.

Location of Turbidity Current	Time	Trigger Mechanism	Trigger Source Temperature	Ambient Temperature of Water Body Along the Movement of Turbidity Currents	Source
Gaoping Canyon	7–10 August 2009	Storms cause high-density floods	Gaoping River temperature: above 28 °C	Sea area: 0–200 m: 30–15 °C 200–500 m: 15–8 °C 500–1000 m: 8–5 °C 1000–4000 m: 5–3 °C	[21,22]
Gaoping Canyon	14–17 September 2016	Storms cause high-density floods	Gaoping River temperature: above 28 °C	Sea area: 0–200 m: 30–15 °C 200–500 m: 15–8 °C 500–1000 m: 8–5 °C 1000–4000 m: 5–3 °C	[23,24]
Eel Bay Canyon	12 January–3 April 2000	Storms, not directly related to river floods	0–100 m: 14–10 °C	Sea area: 100–200 m: 10–9 °C 200–400 m: 9–7 °C 400–1500 m: 7–3 °C	[25,26]
Monterey Canyon	17–19 December 2002	Highly consistent with the storm activity	0–200 m: 14–9 °C	Sea area: 200–500 m: 9–5 °C 500–1500 m: 5–3 °C	[26]
Monterey Canyon	Winter	Failure of canyon head or slope due to sediment accumulation	0–200 m: 14–9 °C	Sea area: 200–500 m: 9–5 °C 500–1500 m: 5–3 °C	[26,27]
Congo Canyon	December 2019–March 2010	Increased flow of high-density rivers	Congo River water temperature: above 26 °C	Sea area: 0–200 m: 30–15 °C, 200–500 m: 15–8 °C Under 500 m: 8–3 °C	[28,29]
Val Canyon	17–19 December 2008 5–8 February 2009	High-density flow during river flooding and some local storms	Annual average temperature of Val River: 17–25 °C	Sea area: 0–510 m: 25–13 °C 510–1280 m: 13–3 °C	[30,31]
Lion Bay Canyon	12 November 2003	Rivers flooded during the storm	0–100 m: 17–16 °C	Sea area: 100–200 m: 16–15 °C 200–300 m: 15–13 °C Under 300 m: 13–3 °C	[32]

Note: There is a negative correlation between the ambient temperature of the water body and an increase in depth along the turbidity current path. The temperature data are supplemented from https://argo.ucsd.edu/data/data-visualizations Ocean data system (accessed on 2 December 2024).

Heat-carrying turbidity currents can transport shallow warm water masses to deep-water areas, generating intense convective mixing, overturning the water column, and releasing dissolved gases into the atmosphere. This can have devastating impacts on fish populations and potentially lead to habitat destruction in the surrounding area, such as degassing events in other so-called "killer lakes" such as Nyos and Monoun [33]. However, there is currently no research on turbulent mixing processes originating from shallow warm turbidity currents, and most previous studies on reverse buoyant flows have been driven by the sedimentation behavior of density flows. For example, Sparks (1993) first investigated sedimentation as the main mechanism leading to a decrease in stacking density during turbulent mixing through experiments [34]. Cantelli (2008) studied turbidity currents generated by underwater volcanic eruptions and investigated the deposition and lofting of two different density and particle size sand suspensions in relatively cold environments, indicating that the lofting process affects downstream mixing and sediment thickness [35]. Gladstone (2010) conducted a sedimentary model study of turbidity current experiments with reverse buoyancy, and an important feature of the results is the non-uniqueness of the deposit structure: different initial current compositions can generate deposits with very similar bed profiles and grading characteristics, highlighting the difficulty of reconstructing mother flow properties from field data [36]. Steel et al. (2016, 2017) conducted field observations and laboratory experiments, indicating that the initial characteristics of turbidity currents can change convective processes, affecting velocity, sediment thickness,

and range [37–40]. Lu (2022) conducted an experiment on sediment-laden rivers into stratified water bodies, dividing turbidity currents into overflows, interflows, or underflows, depending on density contrast, and using dimensionless parameters to describe the velocity characteristics of turbidity convection [41]. Although it is known that the particle size and sediment concentration of turbidity currents significantly affect convective processes (velocity structure, concentration structure, sediment thickness, and range), there is little theoretical research on the mechanism of temperature's impact on turbidity current movement characteristics, and whether shallow heat carried by turbidity currents can cause "pollution" to the stable hydrological environment in deep-water areas. As a result, there is little understanding of this knowledge gap. This knowledge gap reflects a lack of detailed information on the mechanism of turbidity currents carrying shallow heat to deep-water areas and how temperature conditions affect turbidity current convective mixing changes.

This research seeks to explore sediment and thermal transport in turbidity currents, analyzing how the initial characteristics of warm currents affect the stable stratification of aquatic environments and their primary role in turbidity current motion, excluding complex elements such as wind stress and wave action. In particular, we study the effects of dimensionless parameters R_s (the ratio of changes in ambient water concentration due to salinity to sediment load) and R_T (the ratio of changes in ambient water concentration due to temperature difference to sediment load) on the turbulent mixing of turbidity currents. Based on descriptions of warm turbidity current experiments, we explore how the dynamics of turbidity currents depend on the relative contributions of temperature gradient, sediment load, and turbidity current volume. Non-dimensional density ratios R_0 are used to investigate the relative importance of buoyancy-driven and convective motions. By understanding the behavior of warm turbidity currents in laboratory experiments, we use existing environmental entrainment functions E to understand how sediment-driven turbidity currents can lead to stable mixing. A simplified application is to estimate how much heat induced by warm turbidity currents triggered by extreme hydrological events or earthquakes can carry to deeper layers, potentially disrupting stable stratification in lakes or deep oceans. This encourages us to consider the role of turbidity events in thermal transport in bottom channels, which may be an important mechanism for energy exchange in lake and deep-sea environments.

2. Theory

In multiphase gravity flows, the buoyancy of the flow induced by the relative density difference caused by temperature cannot be ignored. This will inevitably affect the movement and mixing of reverse buoyancy turbidity currents. We introduce the density ratio theory proposed by Lu et al. (2022) and consider the contribution of temperature gradients to turbulent mixing and convective processes [40]. Establishing a simplified system helps to understand the dynamic process of rivers entering the receiving environment with sediment and heat, and this model ignores waves' influence on bottom currents' heat transport. The initial density of the turbidity current is ρ_M, the density of ambient water within the turbidity current is ρ_0, and the density of ambient water in the ocean or lake is ρ_E. In addition, the relative contributions of temperature, sediment, and salinity in each layer can be specified according to the following formula:

$$\begin{aligned} \rho_M &= \rho_0 + \Delta\rho_c \\ \rho_E &= \rho_0 + \Delta\rho_s + \Delta\rho_T \end{aligned} \tag{1}$$

Generally, ρ_0 is the initial density of the river, $\Delta\rho_c$ is the increase in sediment density difference, and $\Delta\rho_T$ can increase or decrease the density, such as in the case of a river with high temperature or a glacier river. It should be noted that $\Delta\rho_T$ is the density difference caused by the temperature difference between the river and the ambient water. Therefore, if the river is hotter than the ambient water ρ_E, $\Delta\rho_T$ is positive. The negative sign in the equation remains unchanged. Equation (1) ensures that the temperature contribution

changes ρ_M. $\Delta\rho_c$ is the density difference caused by sediment, which is always positive, and $\Delta\rho_s$ is the density difference caused by salinity, which is also always positive.

From Equation (1), two dimensionless variables can be derived: the first ratio compares the magnitude of temperature differences with the incoming sediment load, defined as:

$$R_T = \Delta\rho_T / \Delta\rho_c \tag{2}$$

The second ratio compares the difference in "freshness" between the environmental water and the river with the incoming sediment load, defined as:

$$R_S = \Delta\rho_s / \Delta\rho_c \tag{3}$$

These two dimensionless parameters can now be used to describe the formation of overflows, interflows, and underflows, as shown in Figure 2. Overflows occur when $\rho_M < \rho_E$ and $1 - R_T < R_S$; interflows occur when $\rho_M = \rho_E$ and $1 - R_T = R_S$, respectively. If the incoming density is $\rho_M > \rho_E$, underflows occur when $1 - R_T > R_S$.

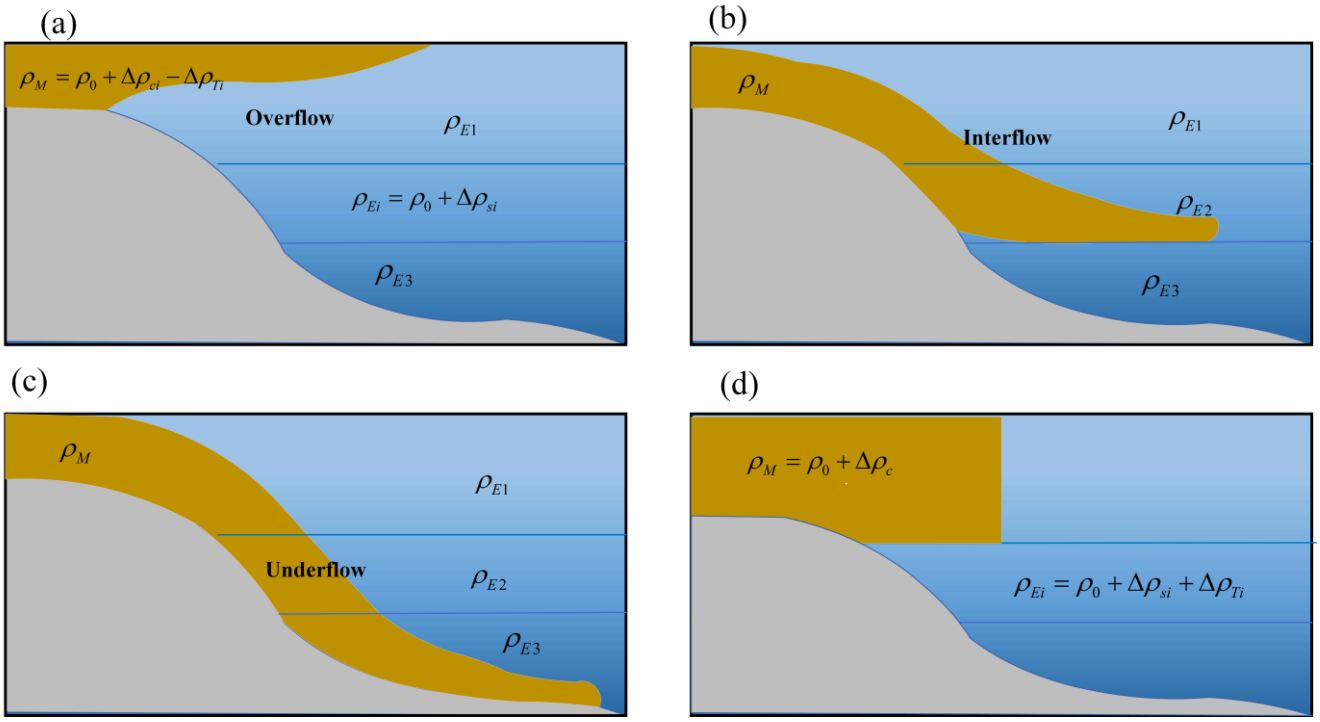

Figure 2. Schematic diagram of three forms of motion of warm turbidity currents entering lakes or oceans. (**a**) Overflow (**b**) Interflow (**c**) Underflow (**d**) Initial state (revised based on research by [40]).

In summary, the new information is first used to estimate when convection may be important in various river plumes. Equations (2) and (3) can be combined to define the following mechanisms:

$$\begin{aligned} &Overflows: R_T + R_S > 1; \\ &Interflows: R_T + R_S = 1; \\ &underflows: R_T + R_S < 1 \end{aligned} \tag{4}$$

Specifically, the convective lofting and environmental mixing activity of turbidity currents are driven by density anomalies generated by sediment load $\Delta\rho_c$ and environmental water density (salinity) $\Delta\rho_s$ as well as water freshness (temperature) $\Delta\rho_T$. When the sediment load disappears, the density of the remaining underflow is now $\rho_M = \rho_0$. Therefore, when ρ_M is less than the density of the lower fluid, i.e., $\rho_0 < \rho_0 + \rho_s + \rho_T$, the rise and mixing of "low-density" substances in the turbid bottom flow and interflow may occur under the following conditions: $0 < R_s + R_T$, which indicates the lower limit of

turbulent mixing rise phenomenon. The interval between the turbidity current bottom current and the interflow during the most severe convective mixing is $0 < R_s + R_T < 1$. So, letting $R_0 = R_s + R_T$, by designing experiments with different R_0 values, the fluid dynamic characteristics of turbidity currents can be studied.

Turbulent mixing at the interface of turbidity currents causes ambient water to be entrained into the turbidity current, thereby diluting the flow. Dilution increases the flow thickness, reduces the flow velocity, promotes sediment settling, changes the distribution of heat and sediment concentration within the turbidity current, and causes changes in the stability of environmental water stratification. Therefore, environmental entrainment (E) directly affects the propagation of turbidity currents by changing the density excess, which can quantify the convective activity in laboratory experiments and is an important dimensional parameter for understanding the convective intensity and heat mixing processes of turbidity currents. Morton et al.'s early work provided a well-known theory that the entrainment rate at any given point in a fluid is proportional to the characteristic velocity at that point [42].

$$E = \frac{w_e}{U} \tag{5}$$

For turbidity currents, entrainment is usually quantified as a dimensionless parameter E, which is expressed as the ratio between the ambient entrainment velocity w_e and the characteristic velocity U of turbidity currents. Jacobson (2014) defined w_e for sediment-laden water flow based on the rate of change A of the cross-sectional area of the water flow [43].

$$w_e = \frac{UdA}{x_f dx_f} \tag{6}$$

where E is the environmental entrainment coefficient; ω_e is the environmental entrainment velocity; U is the velocity of the turbidity current; x_f is the distance of turbidity current migration; and dA is the vertical influence area of turbidity flow. In this study, dA is taken as the envelope area where the temperature exceeds 0.1 °C during the turbidity movement process per unit time.

3. Experimental Design

To simulate the process of turbidity current events carrying shallow heat to the deep sea, indoor experiments were designed to study heat transfer characteristics during warm turbidity current movement, as well as the relationship between initial characteristics (temperature, concentration, volume) and convective motion. A series of lock–release experiments were carried out using a similar apparatus as He (2017) and Han (2022) [44,45], as shown in Figure 3. The system included an acrylic rectangular flume, and a control system for the lock–release inflow. The rectangular flume had a length of 12 m, a width of 0.5 m, and a height of 0.7 m. A slope with a height of 0.25 m and an angle of 4 degrees (refer to the average slope of the continental slope) was placed on the right side of the experimental device. The slope material was made of acrylic board. The lock gate divided the rectangular flume into two parts: the right (upstream) part contained the warm heavy current (sediment–water mixture), and the left (downstream) part filled with homogeneous ambient fluid was composed of pure water at room temperature. In turbidity current preparation, the sum of the volume fractions of the two phases is 1, i.e., $V = \int_V \phi_i dV$, where $\phi = \frac{V_s}{V_s+V_w} = \frac{m_s}{\rho_s(V_s+V_w)}$, so the turbidity concentration (ρ_m) can be expressed as $\rho_m = (1-\phi)\rho_w + \phi\rho_s$, where ϕ is the particle volume fraction; V is the volume of turbidity current; V_s is the volume of sediment; V_w is the volume of water; m_s is the sediment mass; and ρ_s is the sediment density.

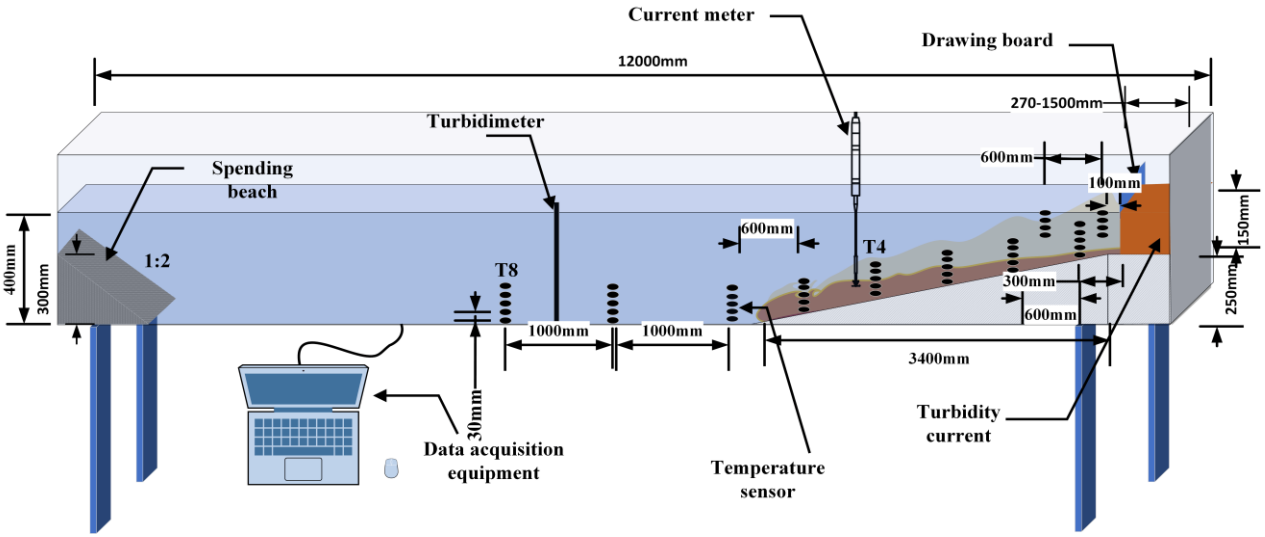

Figure 3. Schematic of experimental device.

Real-time water temperature was collected using temperature sensors (model: PT100) with a frequency of 50 Hz and an accuracy of 0.5%. To monitor the temperature changes caused by convective mixing and lofting during the movement of turbidity currents and their impact on the vertical temperature of ambient water bodies, 10 flow direction sensor groups were established, each consisting of 5 temperature sensors distributed at different positions in the turbulent flow height range (Figure 4a). Previous studies have shown that turbidity flow is mainly composed of silt and clay [15,16,46,47]. Therefore, sedimentary soil from the Yellow River Delta was selected for the experiment, with a median particle size of 0.026 mm and a grading curve shown in Figure 4b.

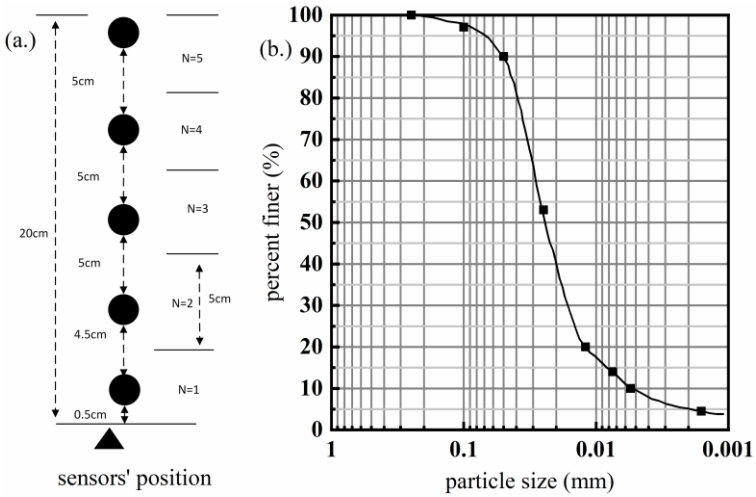

Figure 4. A vertical layout of the sensors and particle grading curve of the experimental soil.

Based on Equation (1), turbidity currents with varying temperatures and volumes were designed and tested, as detailed in Table 2. The purpose of this study is to investigate the factors contributing to the intensity of turbidity currents, including freshwater density, temperature gradient, sediment load, and turbidity current volume. To prepare the warm turbidity current, pure water was uniformly heated to the desired temperature using a heater, which caused a change in $\Delta\rho_T$ [48]. The soil sample was then heated to the same temperature using a constant-temperature electric heating box before being mixed to create the turbidity current. The experiment was conducted in a straight fixed channel, and the channel-slope profile was designed to replicate the actual shape observed in the field. A

comprehensive set of temperature and velocity data was collected from turbidity current experiments to analyze the flow dynamics, entrainment characteristics, and flow evolution of the partially constrained flow.

Table 2. Parameters for experiment conditions.

R_0	Sediment Concentration/ a	$\Delta\rho_c$/kg/m^3	V/L	Turbidity Water Temperature/°C	Freshness of Turbid Water Bodies /kg/m^3	Ambient Water Temperature/°C	ρ_E/kg/m^3	ΔT	$\Delta\rho_c$/ kg/m^3
0.500	0.006	10.00	20	40.80	992.20	25.80	997.20	15.0	5.0
0.100	0.030	50.00	20	40.80	992.20	25.80	997.20	15.0	5.0
0.050	0.062	100.00	20	40.80	992.20	25.80	997.20	15.0	5.0
0.025	0.124	200.00	20	40.80	992.20	25.80	997.20	15.0	5.0
0.017	0.186	300.00	20	40.80	992.20	25.80	997.20	15.0	5.0
0.013	0.186	300.00	20	37.80	993.20	25.80	997.20	12.0	4.0
0.010	0.186	300.00	20	34.80	994.20	25.80	997.20	9.0	3.0
0.007	0.186	300.00	20	31.80	995.20	25.80	997.20	6.0	2.0
0.003	0.186	300.00	20	28.80	996.20	25.80	997.20	3.0	1.0
0.010	0.186	300.00	40	34.80	994.20	25.80	997.20	9.0	3.0
0.010	0.186	300.00	60	34.80	994.20	25.80	997.20	9.0	3.0
0.010	0.186	300.00	80	34.80	994.20	25.80	997.20	9.0	3.0
0.010	0.186	300.00	100	34.80	994.20	25.80	997.20	9.0	3.0

4. Experimental Results

4.1. Temperature Monitoring of Vertical Structural Changes

Upon loosening the lockbox door, the mud instantly collapsed, generating a turbidity current that advanced along the bed. As the turbidity current flowed, it presented a distinct interface with the surrounding water. Turbulent mixing occurred, resulting in curling and expansion backwards. The interface ceased to be distinct, and smaller soil particles remained suspended in the surrounding water. The process is a typical turbidity current, as shown in Figure 5.

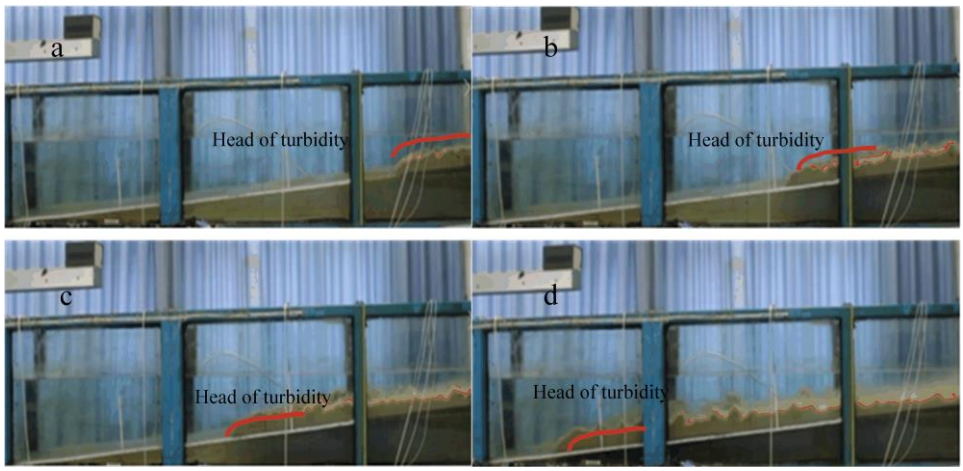

Figure 5. Transport process during the turbidity heat transfer experiment. (**a**–**d**) show the heights of turbidity current flowing through a slope at different times.

The dynamic distribution of the maximum thermal shock temperature through each group of temperature sensors as the turbidity current passes through them is illustrated in Figures 6 and 7. As the turbidity current moved, the temperature value exponentially decreased with height, and the vertical temperature distribution was a nearly empirical power relation, $H = A + B * \Delta T^C$, eventually reaching ambient water temperature. The vertical distribution is like the vertical stratification of sediment concentration in turbidity currents [49]. Some experimental results have been listed, and the remaining experimental groups are presented in Appendix A.

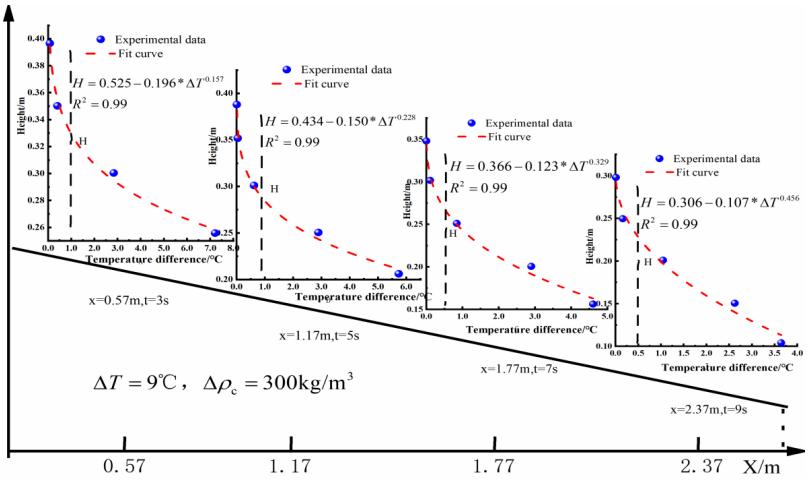

Figure 6. Maximum thermal shock temperature when passing through each group of sensors during turbidity migration (0–2.37 m) under experimental condition $\Delta T = 9$ °C, $\Delta\rho_c = 300$ kg/m^3. (Note: The maximum thermal shock temperature when the turbidity current passes through each group of sensors in the migration process of 2.37–5.57 m is shown in the Appendix A. The red dashed line represents the temperature distribution curve when the turbidity current is transmitted).

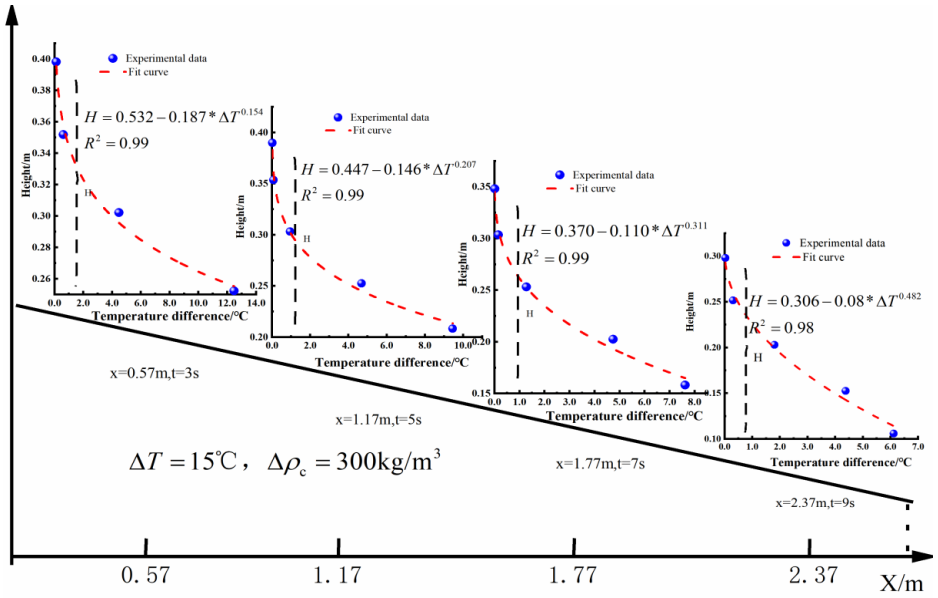

Figure 7. Maximum thermal shock temperature when passing through each group of sensors during turbidity migration (0–2.37 m) under experimental condition $\Delta T = 15$ °C, $\Delta\rho_c = 200$ kg/m^3. (Note: Similar experimental groups are concealed, and the remaining figure is in Appendix A).

4.2. Monitoring the Impact of Temperature on Turbidity Current Motion

To monitor temperature changes during turbidity current movement, an array of temperature sensors was used. The central difference method processed sensor data during the turbulent flow to map turbidity current development. We selected the time ($t = 24$ s) when the turbidity current ($\Delta\rho_c = 300$ kg/m^3, $V = 20$ L) head reached the sensor array $T8$ (5.57 m) to monitor the turbidity current impact range A and calculated the number of environmental entrainments E for consistent calculation. Figures 8–10 show the temperature distribution and influence curve along the centerline of the water tank; the horizontal axis is the distance x in the turbulent flow direction, and the vertical axis is the height H of the turbidity current.

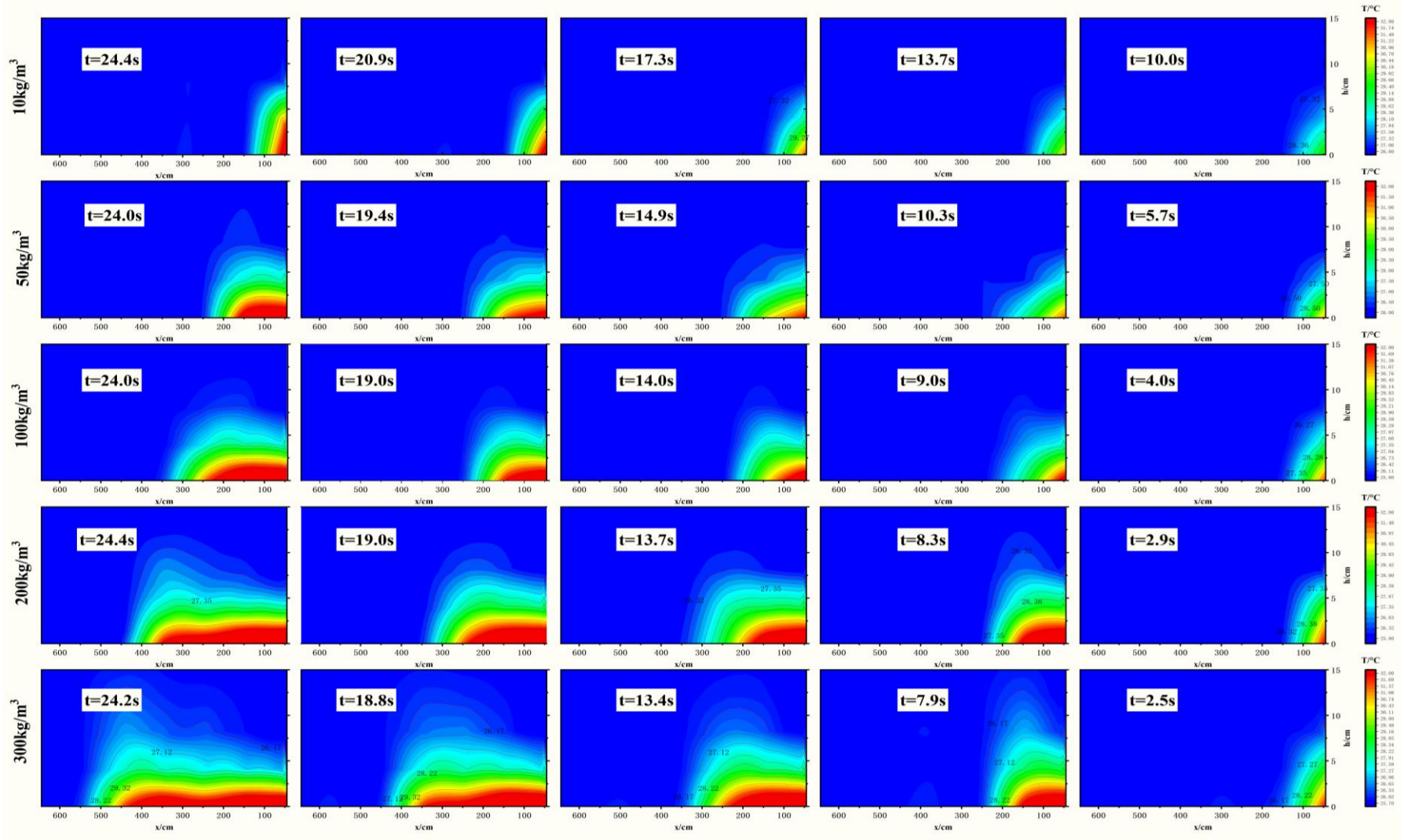

Figure 8. Distribution of temperature profiles and range of influence of turbidity currents of different concentrations 24 s after baffle removal.

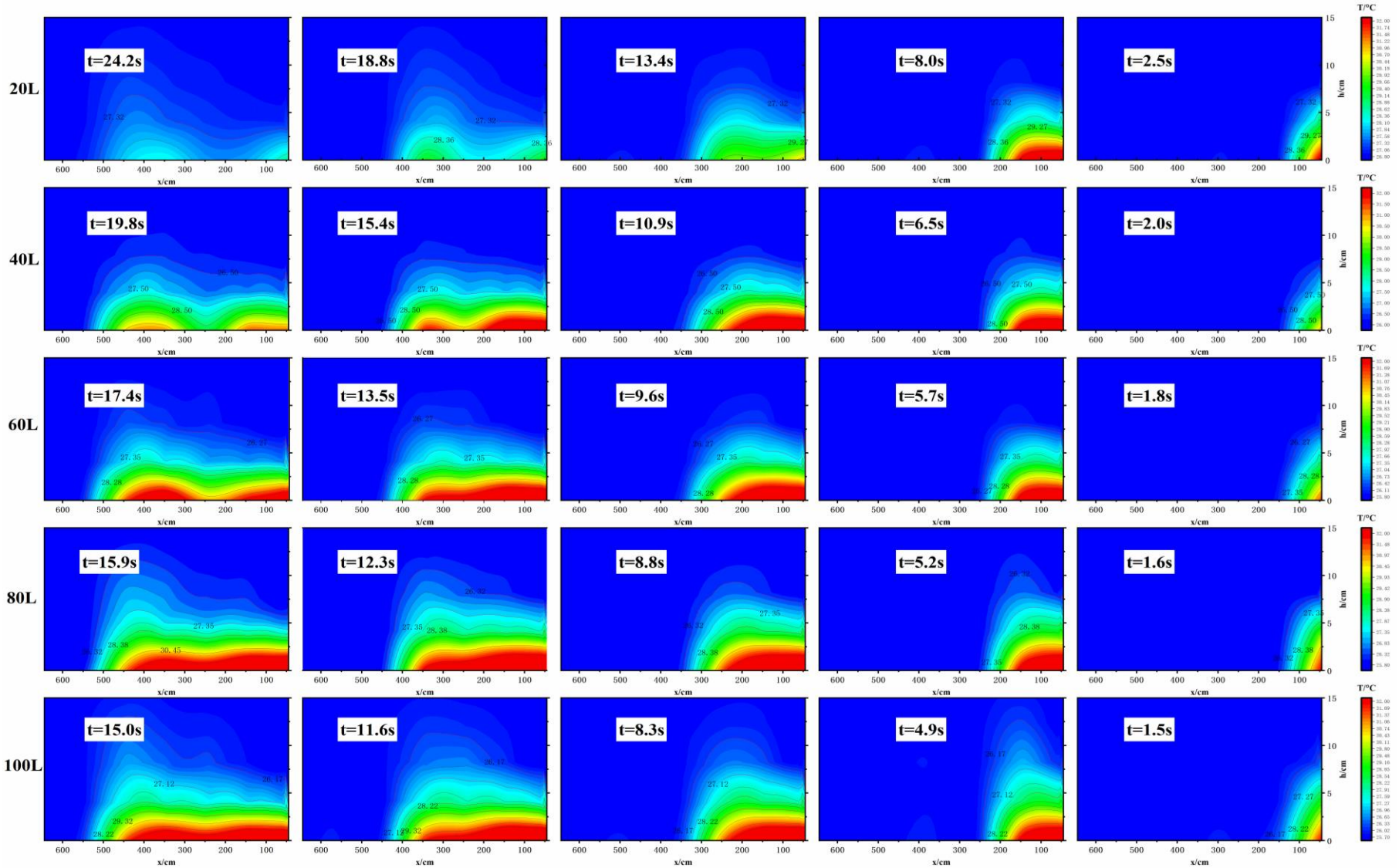

Figure 9. Distribution and influence range of temperature profiles during turbidity flow motion under different temperature differences.

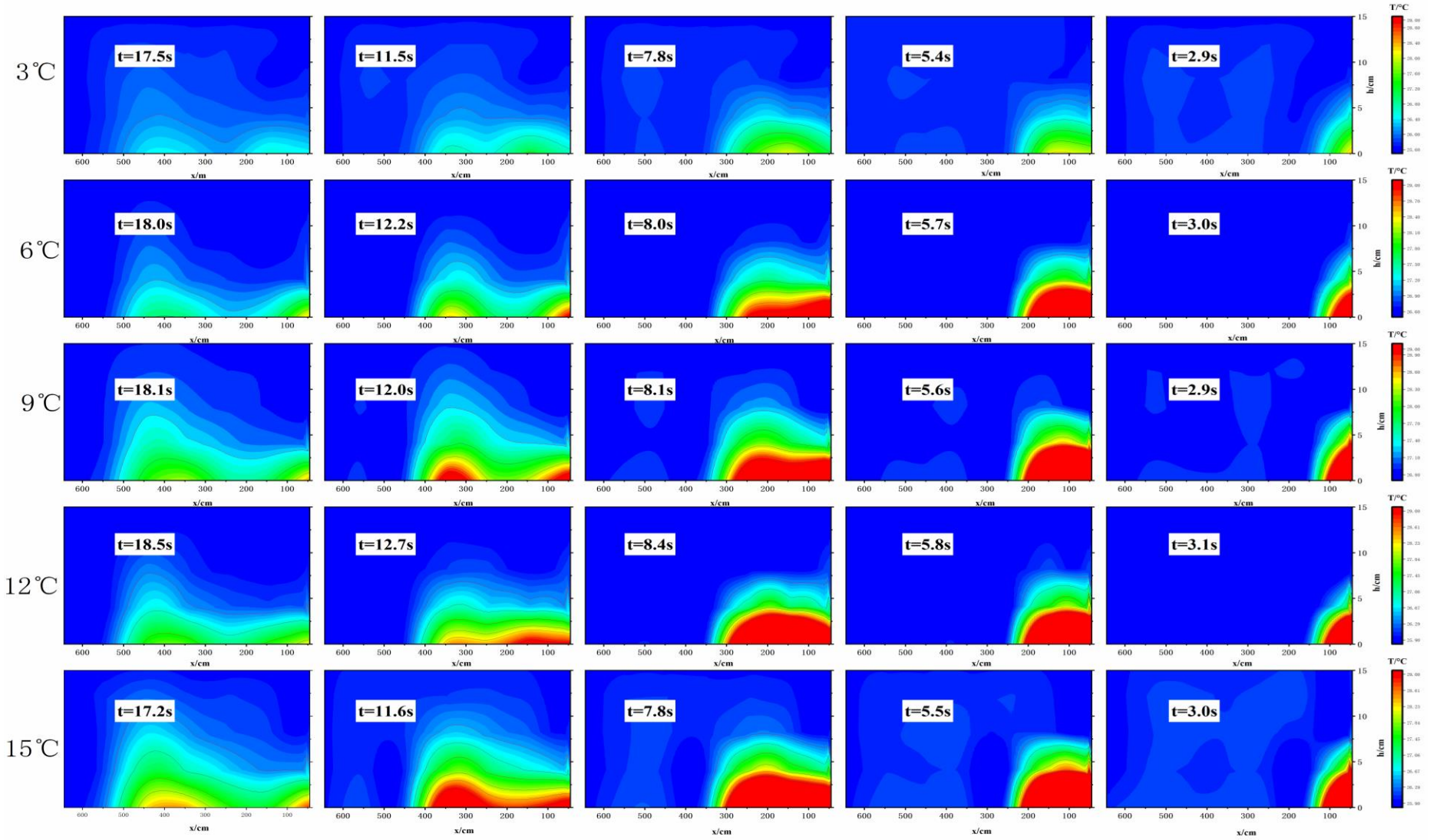

Figure 10. Distribution and influence range of temperature profiles during turbidity flow motion under different temperature differences.

5. Discussion

5.1. Vertical Temperature Distribution in Turbidity Current

Temperature distribution was assessed during all experiments. We selected the temperature variation of the fourth group of sensor arrays ($T4$) in the middle of the flow direction to analyze the vertical structure of temperature during the turbidity current movement process, in order to achieve dimensionless feature calculation of the vertical structure. Normalizing temperature and elevation with depth-averaged temperature and turbidity current thickness, respectively, achieved optimal similarity structure. Mean temperature and mean depth concepts were introduced, and dimensionless experimental data were calculated by normalizing temperature with mean depth using Equation (7). Although there is some variability, the similarity profile represents a good vertical temperature distribution. Figure 8 shows a dimensionless temperature distribution.

$$\Delta T_m = \frac{\int_0^h \Delta T dz}{H} \tag{7}$$

where ΔT_m is depth-averaged temperature, ΔT is the vertical temperature curve, and H is turbidity current height obtained by experimentally fitting the temperature curve, as shown in Figure 11.

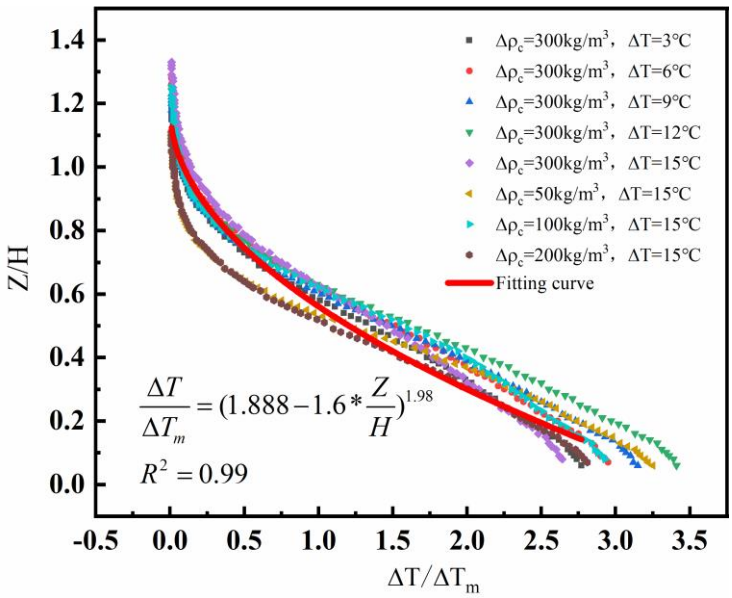

Figure 11. Dimensionless temperature distribution curve during turbidity movement.

To accurately analyze the dynamic heat transfer process of turbidity flows, it is crucial to understand the vertical temperature distribution within them. This study has employed dimensional analysis fitting to determine an empirical power relationship: $\frac{\Delta T}{\Delta T_m} = (1.888 - 1.6 * \frac{Z}{H})^{1.98}$, as shown in Figure 11, which allows us to observe that temperature values decrease exponentially with an increase in height until they equilibrate with their surrounding water bodies. This vertical temperature distribution is like the vertical stratification observed in turbidity currents' sediment concentration [49–51]. Using principles of fluid dynamics and heat transfer, it was possible to determine that vertical dispersion of sediment concentration in a turbidity current was primarily influenced by turbulent mixing and suspension sedimentation, useful insights into entrainment, and effects on the wider oceans. The efficacy of these processes was largely dependent on factors such as the concentration and density distribution of suspended sediments, as well as their particle size. Heat was associated with the sediments and water body of the turbidity sys-

tem, and the movement of the turbidity current was characterized by the following trend: the sediment concentration was high close to the bed bottom in the vertical direction, and the high concentration hindered sedimentation and inhibited turbulence [3], causing the lower half of the turbidity flow to be relatively stable due to lower amounts of convective heat transfer, resulting in the formation of laminar or weakly turbulent high-concentration near-bed layers containing high heat contents [52,53]. In contrast, the particle size and concentration of the sediments in the upper part of the flow profile were small, which allowed for greater degrees of turbulent mixing and convective heat transfer, which also determined the vertical distribution characteristics for heat (Figure 12).

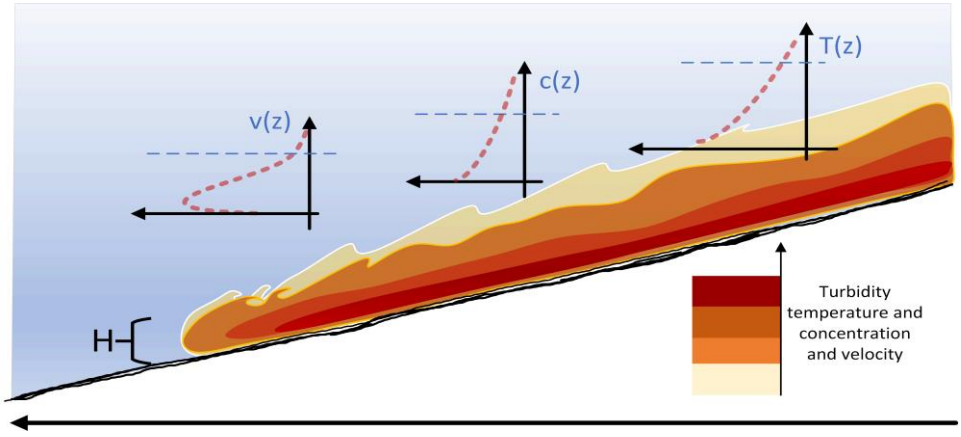

Figure 12. Schematic diagram of heat transport mode and internal temperature distribution of turbidity current in seabed.

A typical heat distribution structure in turbid flow has been summarized, and by performing dimensionless processing through $\frac{\Delta T}{\Delta T_m} = (1.888 - 1.6 * \frac{z}{h})^{1.98}$, it was found that when the turbidity current flowed through each position, the proportion of the heat in the lower half and the total heat flow in that region were always more than 70%, indicating that the heat content of the turbidity current was mainly concentrated in the lower half during the migration process, effectively preserving heat, and areas closer to the bottom bed experienced more heat transfer and greater impact. It can also be theoretically proven that warmed turbidity currents will lead to elevating seafloor temperatures and may trigger the massive release of methane from gas hydrates buried on margins [54,55]. Our experimental results confirmed that the influence of the turbidity current on the bottom bed temperature and heat distribution cannot be ignored.

5.2. The Relationship Between E and Ri

The Richardson gradient number (*Ri*) is a measure of flow stability that controls the mixing rate between turbulent and ambient fluids. It is determined by the ratio of buoyancy gradient to shear and can be used to predict potential convective behavior and mixing velocity of sediment in a river [18,19]. The *Ri* formula is given by:

$$Ri = \frac{g'h}{U^2} \tag{8}$$

where g' is reduced gravity, $g' = g\frac{\rho_{turbidity} - \rho_{ambient}}{\rho_{ambient}}$ U is the average velocity of the flow direction, and h is turbidity current height.

However, previous studies have not considered the relationship between initial turbidity current temperature, turbidity current interstitial fluid concentration, sediment content, and ambient fluid density with *Ri* number [18,49,56]. Based on current indoor experiments, a study was conducted on the relationship between turbidity current stability indicators and environmental entrainment coefficients, considering initial turbidity current tempera-

ture, turbidity current interstitial fluid concentration, and sediment content. The calculation results are shown in Table 3.

Table 3. Calculation of *Ri* and environmental entrainment in each group of experiments.

ΔT/°C	Migration Distance/m	Time/s	Velocity/m/s	Turbidity Concentration /kg/m^3	Reduced Gravity /g′	Turbidity Current Height/m	*Ri*	*E*
3.0	5.52	24.0	0.23	1297.00	2.996	56.421	4.231	0.004
6.0	5.52	24.0	0.23	1296.00	2.986	56.233	4.217	0.013
9.0	5.52	24.0	0.23	1295.00	2.976	56.044	4.203	0.017
12.0	5.52	24.0	0.23	1294.00	2.966	55.855	4.189	0.019
15.0	5.52	24.0	0.23	1293.00	2.956	55.667	4.175	0.021
15.0	4.80	24.0	0.20	1193.00	1.954	49.275	3.695	0.025
15.0	3.36	24.0	0.14	1093.00	0.952	45.961	3.447	0.036
15.0	2.40	24.0	0.10	1043.00	0.451	44.701	3.352	0.055
15.0	1.44	24.0	0.06	1003.00	0.050	15.682	1.176	0.104
9.0	6.72	24.0	0.28	1295.00	2.976	0.0750	4.203	0.018
9.0	7.68	24.0	0.32	1295.00	2.976	0.0753	4.203	0.017
9.0	8.40	24.0	0.35	1295.00	2.976	0.0751	4.203	0.016
9.0	8.88	24.0	0.37	1295.00	2.976	0.0756	4.203	0.015

The environmental entrainment rate is a key factor in the spatial and temporal development of fluids, which can help explain why turbidity currents can travel thousands of kilometers [57]. We consider temperature conditions within the range of fluid motion stability and analyze whether temperature (carrying shallow heat in turbidity currents) affects the convective intensity of turbidity currents (environmental entrainment coefficient *E*). Figure 13 shows the relationship between the environmental entrainment coefficient *E* and *Ri* considering temperature effects, as shown in $E = \frac{0.129-0.028*Ri}{1-0.07*Ri}$. The turbidity current flow considering the influence of temperature conforms to the traditional Turner (1986) form [58], but the values are different, showing that turbidity currents carrying shallow heat (relatively high temperature) can affect convective flow and environmental mixing during motion. We consider the influence of temperature on the buoyancy reversal points of turbidity currents after a certain distance of movement and the convective mixing characteristics of turbidity currents and explain that the similarity of bed characteristics with "classical" turbidity currents have positive significance. Therefore, in turbidity current events carrying shallow heat to the deep sea, temperature conditions cannot be ignored in the study of fluid dynamics of turbidity currents. Unfortunately, the *Ri* number cannot demonstrate the role and importance of temperature conditions.

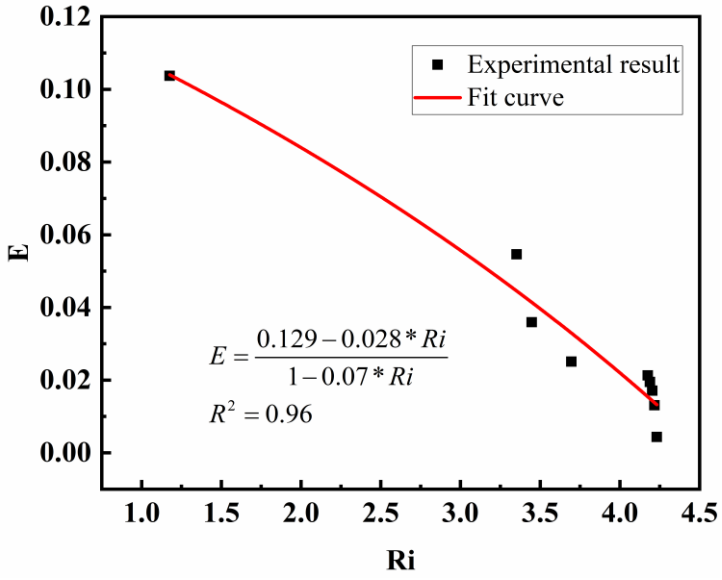

Figure 13. The relationship between environmental entrainment coefficient and Richardson number.

5.3. The Relationship Between E and R_0

The relationship between E and R_i mentioned above cannot characterize the potential convective behavior and convective intensity (entrainment coefficient) of turbidity currents, nor can it reflect the influence of temperature conditions on the characteristics of turbidity current motion. Therefore, using the dimensionless density function R_0 established earlier, the functional relationship between the dimensionless density function R_0 and the environmental entrainment coefficient E is analyzed to intuitively express the role of temperature conditions in turbidity current convective behavior and quantitatively analyze the intrinsic relationship between temperature conditions and convective intensity during turbidity current motion.

When considering the effect of temperature on convective mixing of turbidity currents, as expected, turbidity currents with lower initial temperatures are more conservative in terms of environmental entrainment and convective mixing from the source compared to high-temperature turbidity currents (Table 4). This is because the smaller temperature difference results in a smaller density difference between the interstitial fluid in the initial turbidity current and the surrounding water body, leading to more stable environmental entrainment during the progressive settling process of particles and less likelihood of generating large environmental convective mixing entrainment. Therefore, the relatively stable turbulent motion of the turbidity current is maintained for a longer period of time. Similarly, turbid flow environments with larger temperature differences and lighter interstitial fluids have higher entrainment coefficients (Figure 14) and are closer to the "source" for mixing and diffusion than flows where temperature differences have less impact on interstitial fluid concentration. These results are consistent with previous research on turbidity currents [34,53].

Table 4. Calculation of R_0 and environmental entrainment in each group of experiments.

R_0	x_f	dA	U	ω_e	E
0.0033	5.3000	4.8463	0.2304	0.0010	0.0044
0.0067	5.3000	4.8463	0.2304	0.0030	0.0131
0.0100	5.3000	4.8463	0.2304	0.0039	0.0171
0.0134	5.3000	4.8463	0.2304	0.0045	0.0195
0.0167	5.3000	4.8463	0.2304	0.0049	0.0213
0.0250	4.5700	0.5254	0.1987	0.0050	0.0250
0.0500	3.3100	0.3935	0.1439	0.0052	0.0359
0.1000	2.3100	0.2915	0.1004	0.0055	0.0546
0.5000	1.3000	0.1753	0.057	0.0059	0.1037

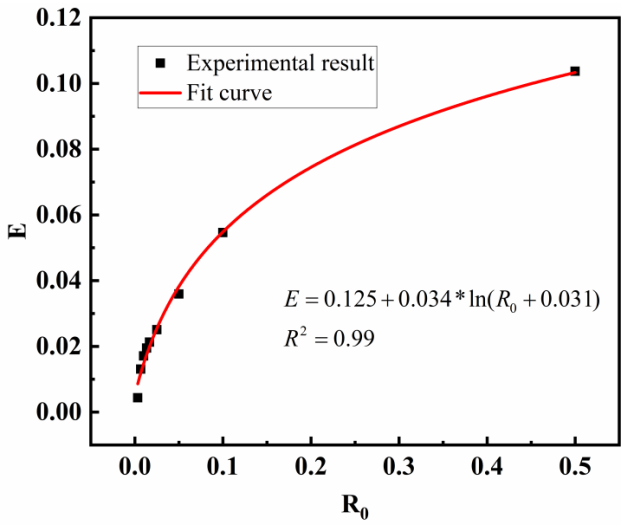

Figure 14. The relationship between environmental entrainment coefficient and R_0.

Two simple dimensionless parameters, R_s and R_T, can fully explain the flow behavior of various turbidity currents and effectively describe the dimensionless functional relationship between turbidity current convection intensity and R in different states. Figure 14 shows that the relative intensity of mixed diffusion and turbulent mixing of turbidity currents depends on R_0, which is the influence of the "temperature and salinity" of turbidity currents, sediment content, and surrounding water density on environmental entrainment. The positive correlation trend between R_0 and convective intensity E is analyzed, and the functional relationship is $E = 0.125 + 0.034 \ln(R_0 + 0.031)$. Therefore, the equations of these two key dimensionless parameters can not only quantify the influence of temperature or salinity on the convective layout and turbulent mixing of the source turbidity current but also reflect that the heat carried by the turbidity current will migrate to deeper water areas, changing the stable thermal stratification of the surrounding water.

5.4. Implications and Hypotheses of Turbidity Currents in Marine Environments

To describe the ability of turbidity currents to carry their own heat with different temperature differences and volumes, nine sets of experiments were analyzed. After the turbidity currents flowed over a slope of 5570 mm, the heat carried by the turbidity currents and the initial heat of the turbidity currents were treated as dimensionless. To simplify the calculation, the measurement values of the eighth group of sensors were taken as the average temperature value of each layer in the plane section, and the density of the turbidity current was estimated to be 1000 kg/m^3. The calculation results are shown in Table 5.

$$\phi_i = \frac{Q_i}{Q_0} = \frac{\sum_{1}^{5} \int_{0}^{t} \rho_w v_{TC} dh_{TC} c_w \Delta T d\tau}{\rho_0 V c_0 \Delta T_0} \quad (9)$$

where ϕ_i is the percentage heat content in each layer relative to the total heat content when the turbidity current flows through an interface; Q_i is heat; ρ is fluid density; c is the specific heat of fluid, $c_0 = c_s a - (1 - a) c_w$; and V is fluid volume. When the turbid current flows through each layer of an interface, the density and velocity adopt the average value in the vertical direction, where v is the fluid velocity; ΔT is the instantaneous temperature difference between the layer of the turbidity current and the surrounding water body; d is the interface width; and t is the time taken for the turbidity current to pass through the interface.

Table 5. Calculation of heat transfer efficiency of turbidity current.

Turbidity Volume/ L	Turbidity Concentration /kg/m^3	ΔT	c_w/J/(kg·K)	c_s/J/(kg·K)	Initial Heat/kJ	Heat Flux at 5.57 m/kJ	Heat Transport Efficiency/ ϕ
20	1295	3	4182	1182	286.791	38.717	0.135
20	1295	6	4182	1182	573.581	115.8637	0.202
20	1295	9	4182	1182	860.372	212.512	0.247
20	1295	12	4182	1182	1147.163	308.587	0.269
20	1295	15	4182	1182	1433.953	559.242	0.39
40	1295	9	4182	1182	1720.744	578.170	0.336
60	1295	9	4182	1182	2581.116	1022.122	0.396
80	1295	9	4182	1182	3441.488	1369.712	0.398
100	1295	9	4182	1182	4301.860	1772.366	0.412

Indoor experiments allow the visualization of natural turbidity events flowing into lakes or oceans by initiating and developing turbidity currents with similar behavior. In fluid dynamics, flow similarity generally requires geometric similarity, motion similarity (Reynolds number criterion), and dynamic similarity (Froude criterion), but it is difficult to achieve both flow similarity and motion similarity simultaneously due to turbidity currents being gravity-driven flows where gravity acts on suspended sediment particles.

Therefore, the dynamic similarity of turbidity currents is mainly conserved by the Froude similarity [59]. Meanwhile, the Froude (Fr) similarity has a long history in designing laboratory-scale hydrodynamic models, such as rivers, spillways, debris flows, and turbidity currents [60,61].

$$Fr = \frac{U}{\sqrt{g'h}} \tag{10}$$

$$\frac{L_1}{L_2} = \lambda_L, \frac{g'_1}{g'_2} = \lambda_{g'}, \frac{U_1}{U_2} = \sqrt{\lambda_L \lambda_{g'}} \tag{11}$$

Turbidity current events triggered by high-density river floods or earthquakes usually flow along the riverbed, so the influence of waves, wind speed, etc., is not considered. The Froude similarity criterion is used to estimate how much heat turbidity currents can carry into deeper areas, to evaluate the impact of actual turbidity current events on environmental water bodies. In this study, turbidity currents are approximated as conservative flows (e.g., density flows of high-speed turbulence or saltwater flows), and the sediment setting velocity can be set to zero. On the premise of maintaining geometric similarity and dynamic similarity, a turbidity current with a volume of 1.6×10 m^3, an initial height of 50 m, an initial sediment concentration of 80 kg/m^3, and a velocity of 5 m/s can still carry its own 10% heat into deeper waters after moving 2120 m on a 4° slope with a temperature difference of 3 °C from the ambient water (the scaling ratio is $\lambda_L = 400, \lambda_{g'} = 1.23$). Meanwhile, a turbidity current with a volume of 8×10 m^3 and the same flow conditions can carry more than 42% of its own heat into the deep sea with a temperature difference of 9 °C from the ambient water. The scaling of operating conditions based on laboratory conditions belongs to the ideal state, but this reflects that turbidity currents have good heat-carrying efficiency, which is in the same order of magnitude as the heat-carrying efficiency of real turbidity current events calculated by Tian's numerical calculation [9]. These results lead to some predictions and hypotheses about temperature changes and the original energy distribution of the deep-sea system, encouraging us to consider the role of turbidity current events in heat transport in the seabed channel, which may be a mechanism for temperature changes in the deep-sea environment.

It should be noted that the influence of wave action on the heat-carrying characteristics of turbidity currents was ignored in this study. Although changes in wave amplitude have no significant effect on the propulsion of turbidity currents and do not change their velocity, wave motion causes a "piston-like" oscillation in the vertical concentration distribution of turbidity currents [62–64]. Perhaps waves play an indispensable role in the transport of heat carried by turbidity currents in shallow waters [65,66], and future research will take wave factors into account to further study the impact of wave action on environmental entrainment during turbidity current heat transport.

A single turbidity current event (submarine sediment density flow) can transport over 100 km^3 of sediment [67–69], ten times the annual sediment flux from all of the world's rivers [3,70]. These flows are the longest sediment density flows recognized on Earth and can achieve prodigious run-out distances of more than 1500 km, also inputting large amounts of heat and mass to marine environments over long periods of time via long-distance migration. From limited field data on deep-sea turbidity currents, the temperature of deep-sea environment water rises during turbidity current events, indicating that a large amount of high-temperature heat in the source area moves with the turbidity flow towards the deep-sea environment. The published data show that turbidity currents reaching 1020–1445 m water depth increase the ambient temperature by 2–3 °C [26], even 1–2 °C at 3000 m water depth [71], which changes the original heat distribution of submarine channels, deep-sea canyons and deep-sea plains, significantly affecting changes in the temperature and original heat distribution of marine environments, as shown in Figure 1. Therefore, the increase in the frequency and intensity of turbidity currents driven by future climate change may have a significant impact on the organic matter supply of deep-sea ecosystems and the heat stored in continental margins and ocean basins. As an indispensable part of the marine environmental system, turbidity currents carrying heat into the sea need to be further studied in

future research on marine sedimentary geology, marine environmental pollution, and ocean heat distribution.

6. Conclusions

1. We quantitatively describe the convection and environmental mixing dynamics of shallow high-temperature turbidity currents at different sediment concentrations using the environmental entrainment coefficient E and summarize the relationship between the environmental entrainment function E and Ri considering temperature effects: $E = \frac{0.129-0.028Ri}{1-0.07Ri}$. Two simple dimensionless parameters Rs, R_T effectively describe flow factors and flow patterns during turbidity current motion. These two parameters quantify the ratio of temperature, salinity, and sediment content, summarize the relationship between the dimensionless density ratio R_0 reflecting turbidity current convection and environmental mixing and the environmental entrainment number E: $E = 0.125 + 0.034\ln(R + 0.031)$ and describe the impact of upper warm turbidity currents on the stable stratification of lake or coastal marine environments.
2. During the heat transport process of turbidity currents, the temperature distribution in the vertical direction is exponential: $\Delta T/\Delta T_m = (1.89 - 1.6 \times z/H)^{1.98}$, and 70% of the heat is concentrated in the lower half of the turbidity current for rapid transport, making the turbidity current efficiently store transported heat, reducing the vertical convective heat transfer loss, and facilitating the long-range transport of heat carried by turbidity. The continuous input of the turbidity current will be accompanied by a large amount of energy transfer, which will affect the temperature distribution in the regional marine environment.
3. Heat transfer at the sea–air interface has difficulty changing the energy distribution in the deep sea, and the effect of turbidity currents is opposite to the effect of river-to-ocean heat transfer or ocean surface-to-bottom heat transfer, directly affecting the thermal distribution of the internal or underpart of the ocean environment. The introduction of upper-layer heat into the deep sea by turbidity currents is an important component of the global heat transfer system that cannot be ignored, and it is also a complement to the heat transfer process of the global heat transfer system.

Author Contributions: Writing—original draft, H.T.; Writing—review & editing, G.X., J.Z., Y.R. and H.W. All authors have read and agreed to the published version of the manuscript.

Funding: This project was provided by the Qingdao Postdoctoral Funding Project (No. QDBSH20240202079), National Natural Science Foundation of China (No. 41976049), China Marine Geological Survey Project (No. DD20243114) and Natural Science Foundation of Shandong Province (No. ZR2021MD074).

Data Availability Statement: The sea surface temperature and marine water temperature data were obtained from hydrological monitoring platforms (https://argo.ucsd.edu/data/data-visualizations), and the ambient water temperature in the trigger source area data were derived from the following resources available in the public domain [20–31]. Data sets for this research are available at this site (https: //doi.org/10.5281/zenodo.8008740).

Acknowledgments: We would like to thank graduate students Zhiyuan Chen, Meng Li, Zihan Zhang, and Cheng Zirui for their help with sampling and sample processing. In addition, we would also like to thank the experts of the "Hanhai inspirational" academic forum of College of Marine Geosciences, Ocean University of China, for their help in revising the paper.

Conflicts of Interest: The authors declare no conflict of interest.

Appendix A

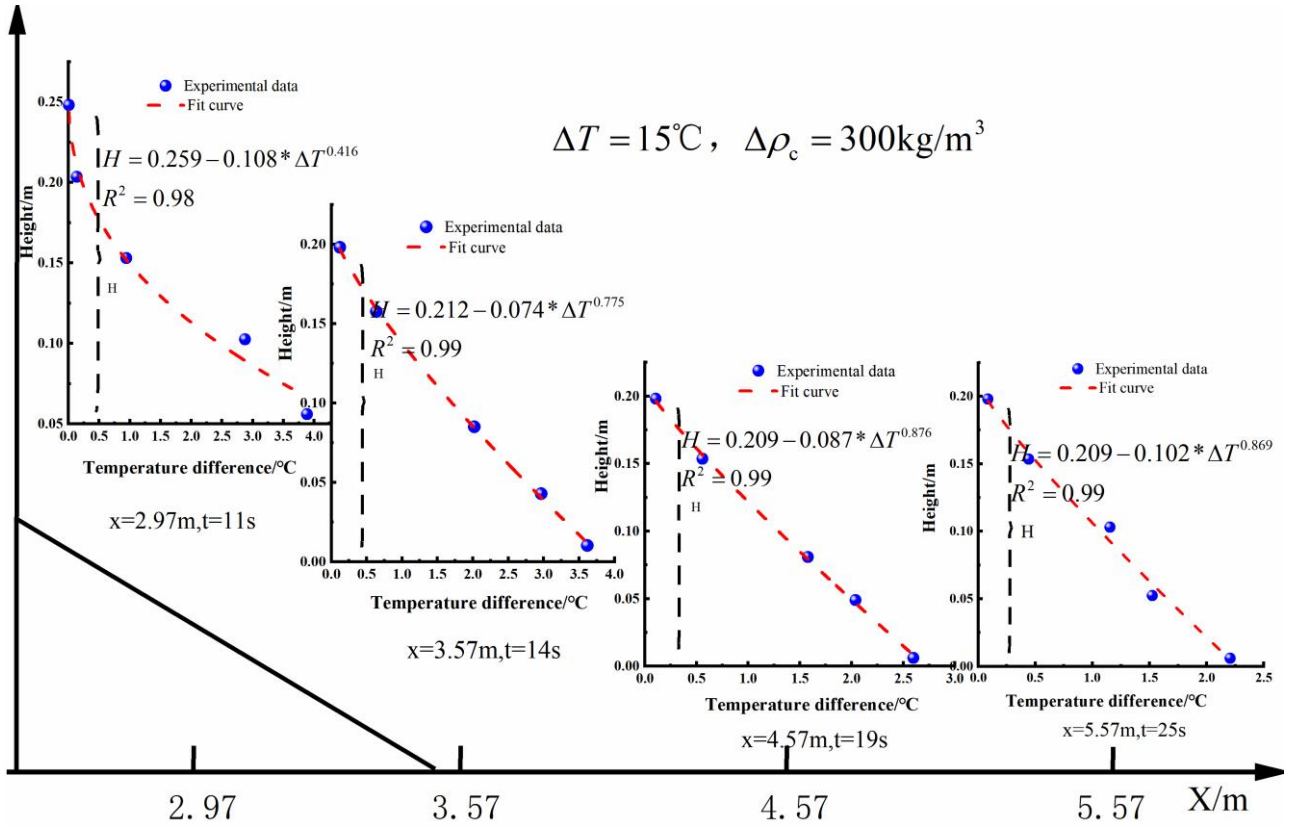

Figure A1. Maximum thermal shock temperature when passing through each group of sensors during turbidity migration (2.37–5.57 m) under experimental condition $\Delta T = 15$ °C, $\Delta\rho_c = 300$ kg/m^3.

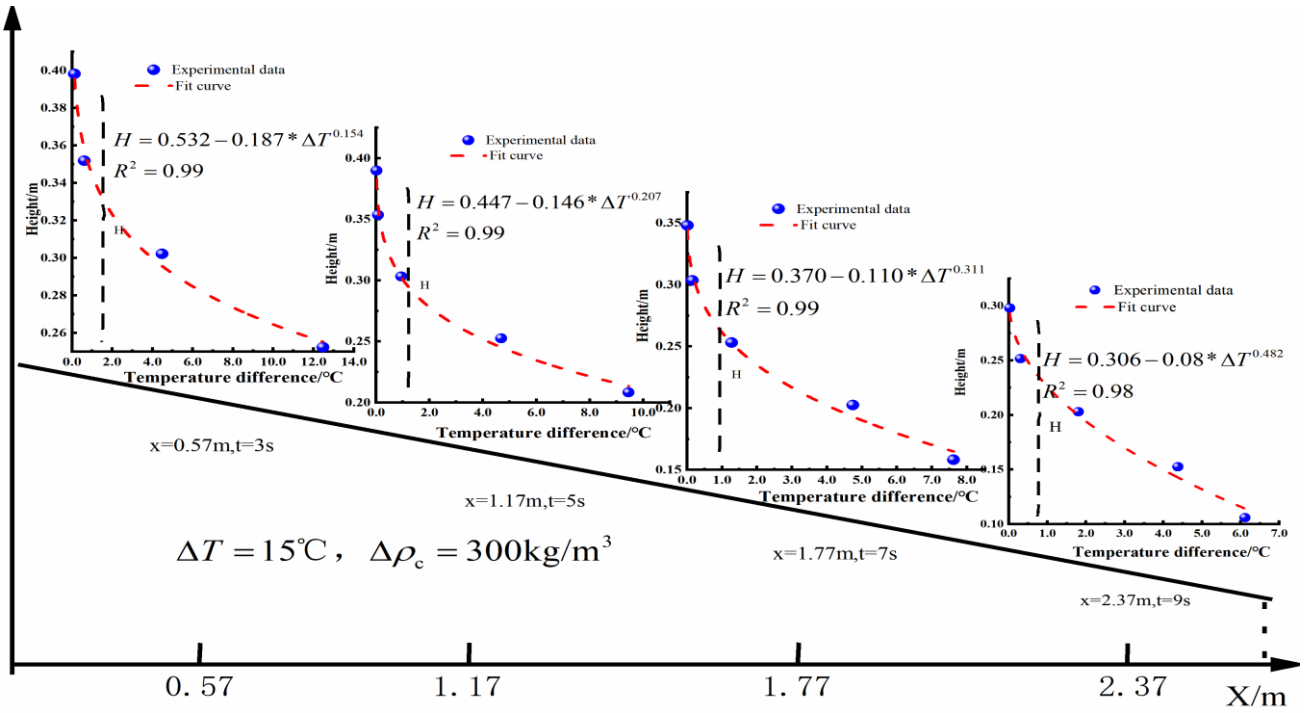

Figure A2. Maximum thermal shock temperature when passing through each group of sensors during turbidity migration (0–2.37 m) under experimental condition $\Delta T = 15$ °C, $\Delta\rho_c = 300$ kg/m^3.

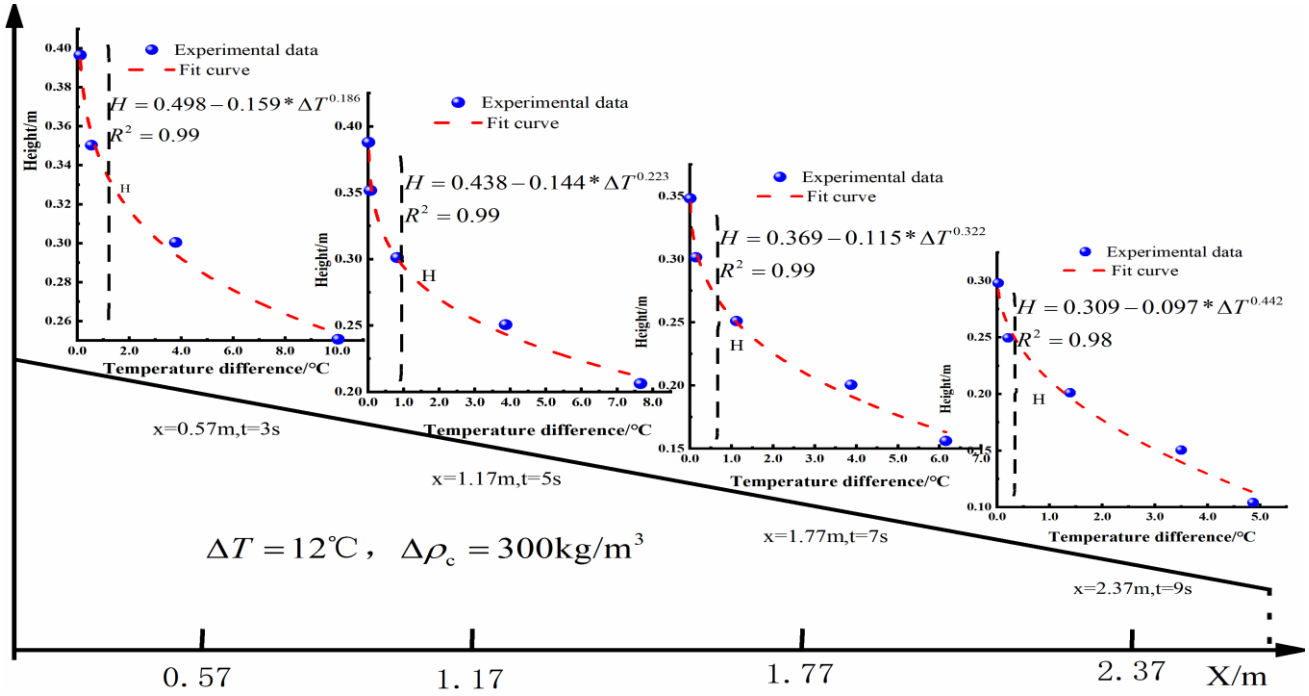

Figure A3. Maximum thermal shock temperature when passing through each group of sensors during turbidity migration (0–2.37 m) under experimental condition $\Delta T = 12$ °C, $\Delta\rho_c = 300$ kg/m^3.

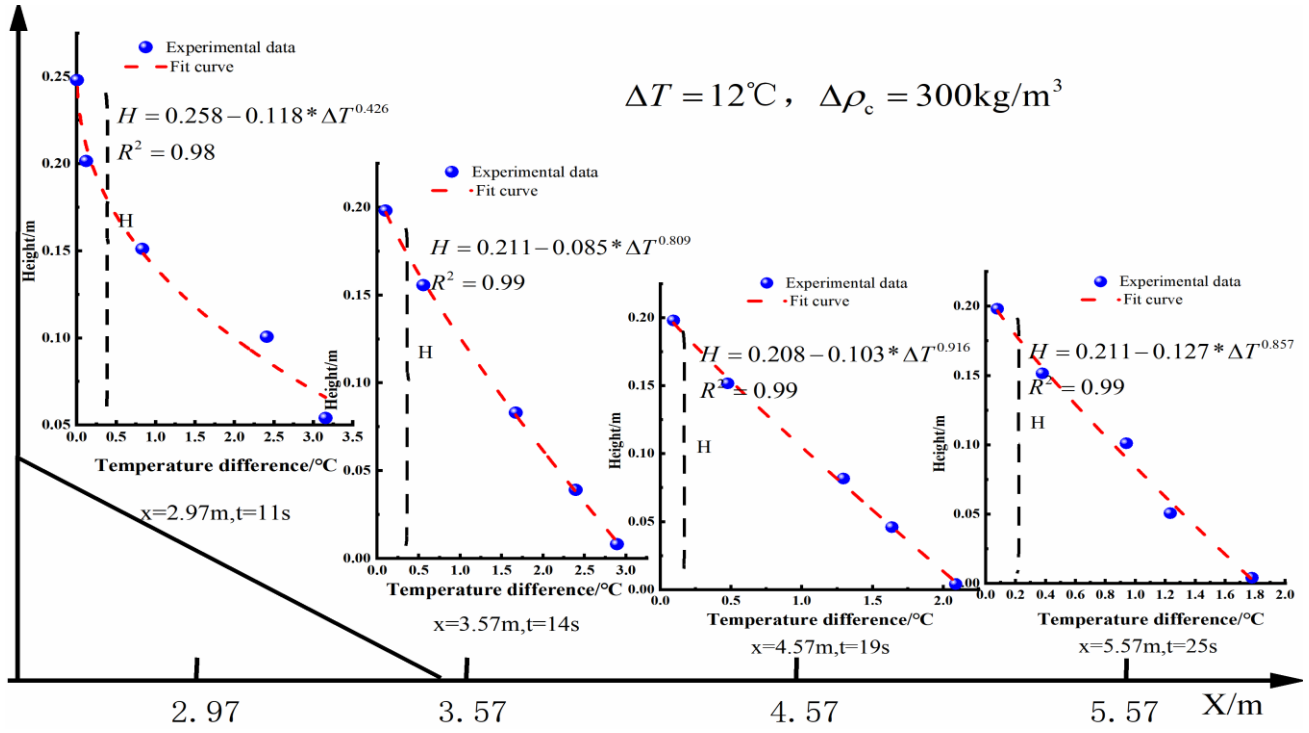

Figure A4. Maximum thermal shock temperature when passing through each group of sensors during turbidity migration (2.37–5.57 m) under experimental condition $\Delta T = 12$ °C, $\Delta\rho_c = 300$ kg/m^3.

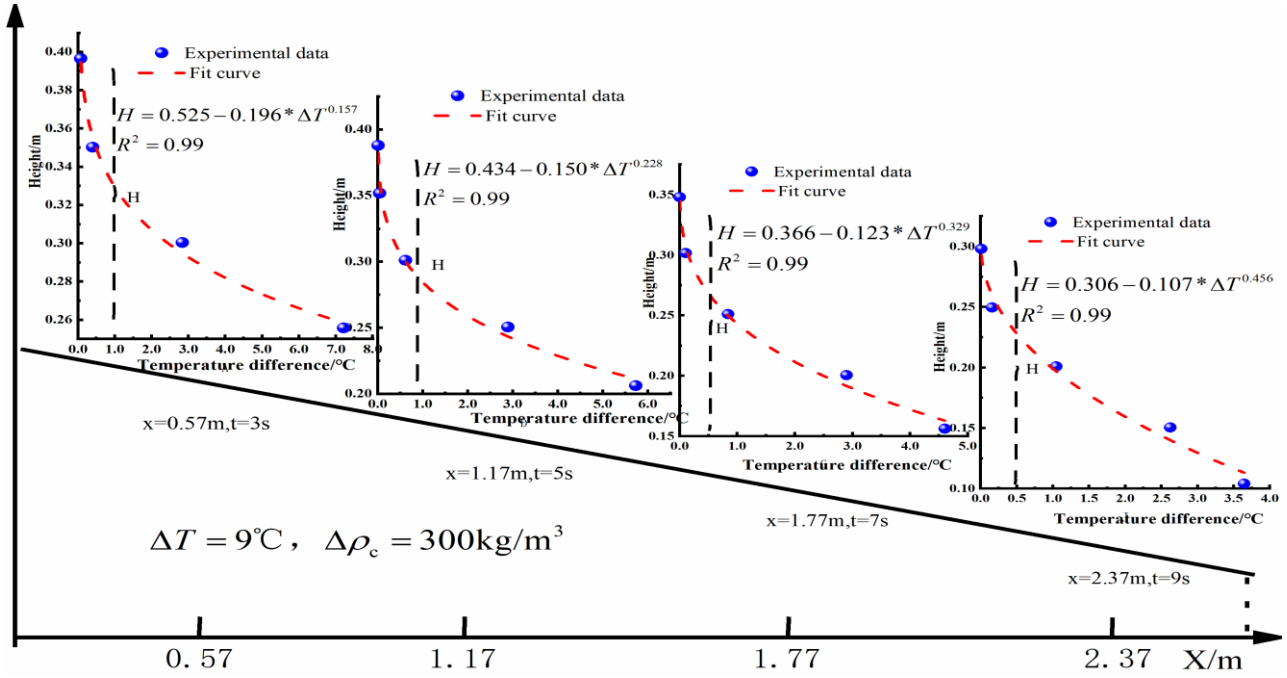

Figure A5. Maximum thermal shock temperature when passing through each group of sensors during turbidity migration (0–2.37 m) under experimental condition $\Delta T = 9$ °C, $\Delta\rho_c = 300$ kg/m^3.

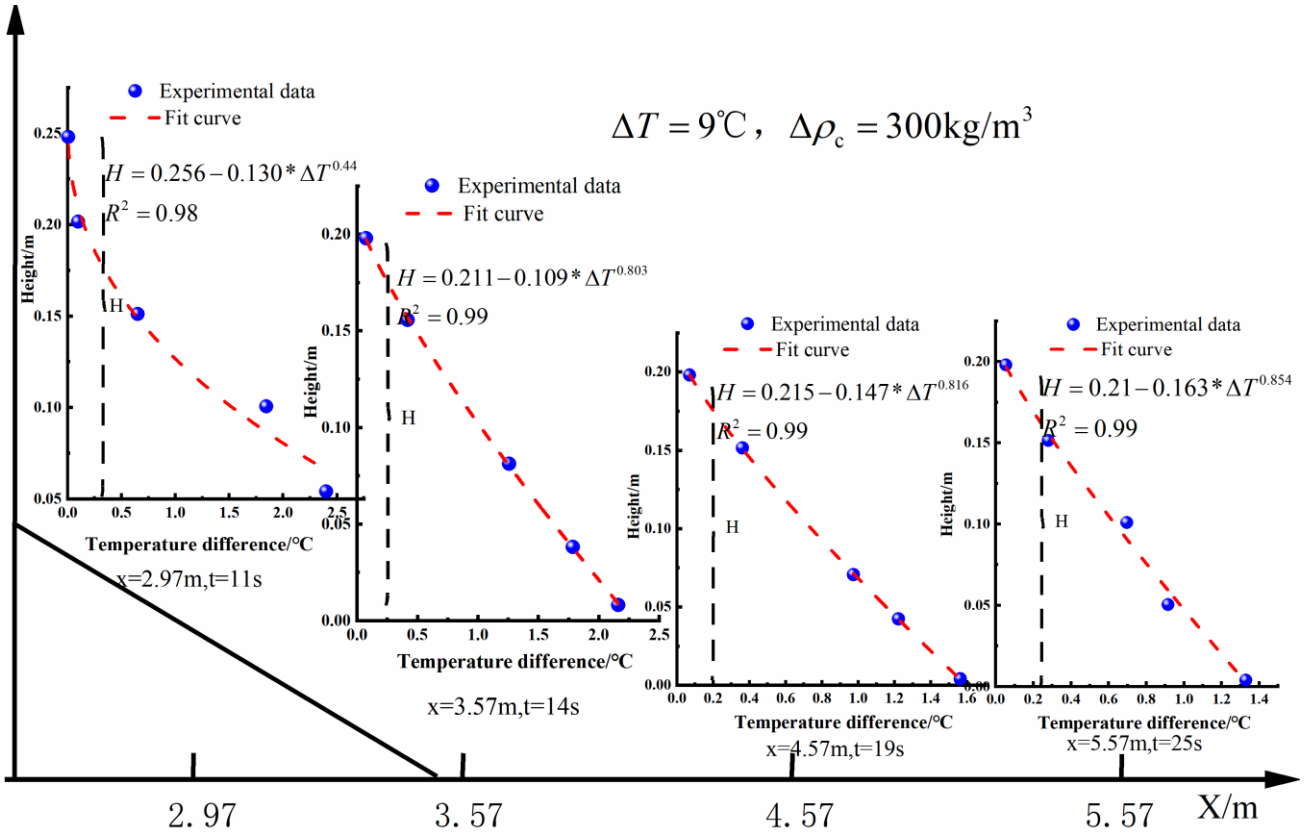

Figure A6. Maximum thermal shock temperature when passing through each group of sensors during turbidity migration (2.37–5.57 m) under experimental condition $\Delta T = 9$ °C, $\Delta\rho_c = 300$ kg/m^3.

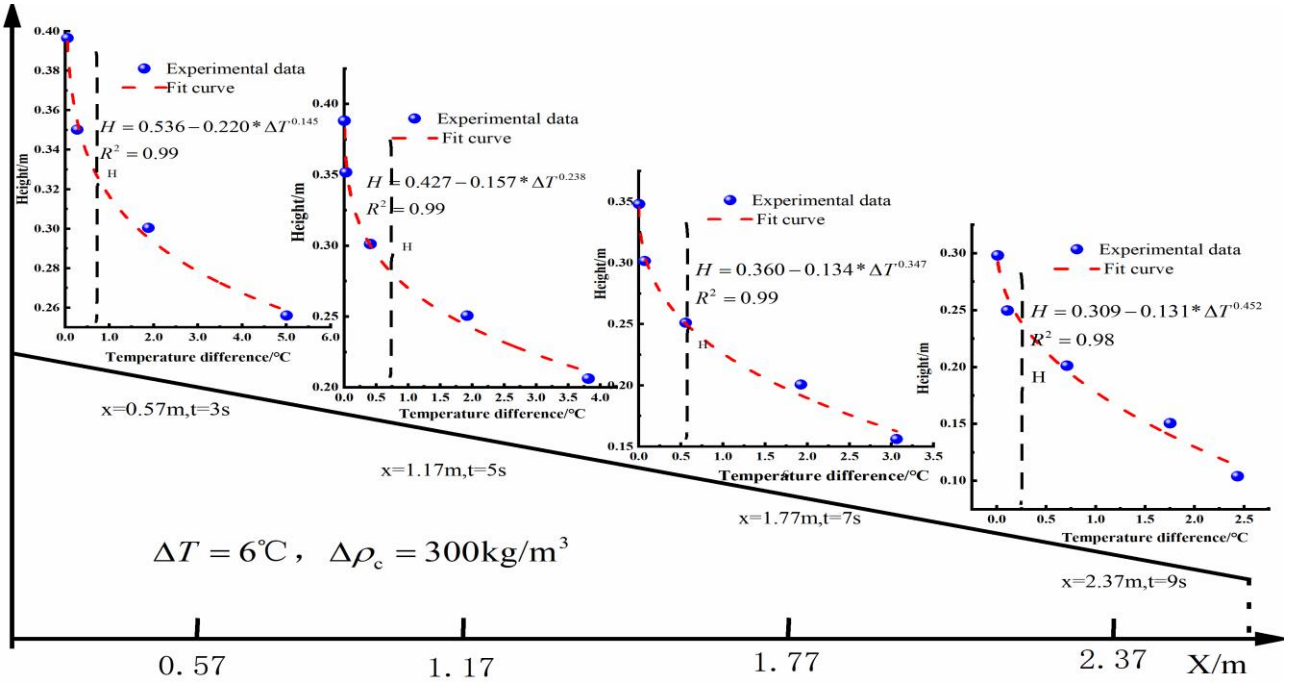

Figure A7. Maximum thermal shock temperature when passing through each group of sensors during turbidity migration (0–2.37 m) under experimental condition $\Delta T = 6$ °C, $\Delta\rho_c = 300$ kg/m^3.

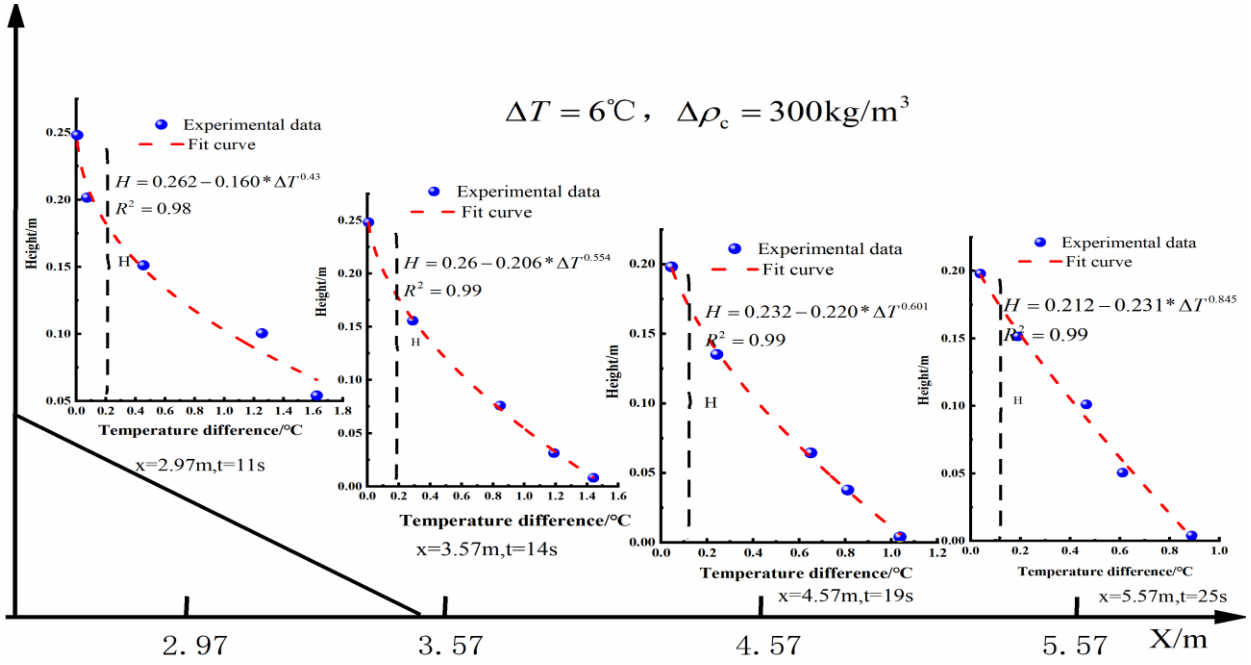

Figure A8. Maximum thermal shock temperature when passing through each group of sensors during turbidity migration (2.37–5.57 m) under experimental condition $\Delta T = 6$ °C, $\Delta\rho_c = 300$ kg/m^3.

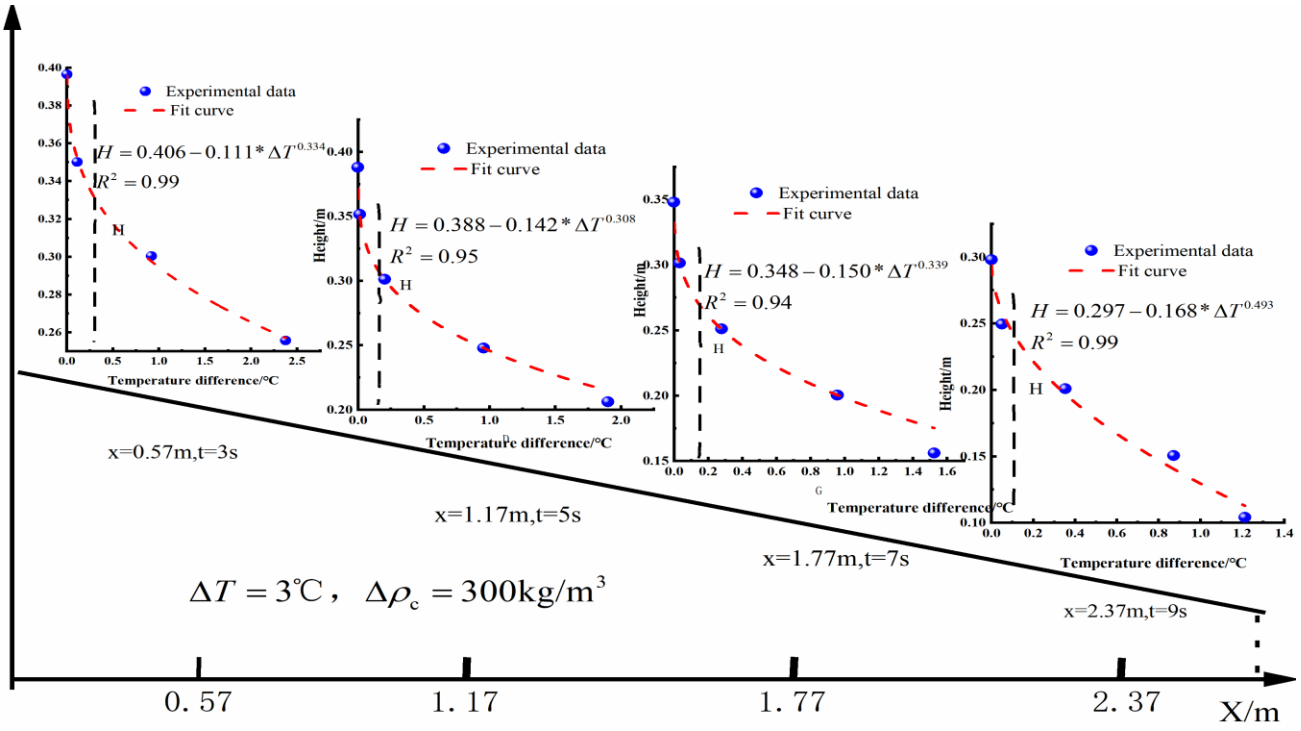

Figure A9. Maximum thermal shock temperature when passing through each group of sensors during turbidity migration (0–2.37 m) under experimental condition $\Delta T = 3$ °C, $\Delta\rho_c = 300$ kg/m^3.

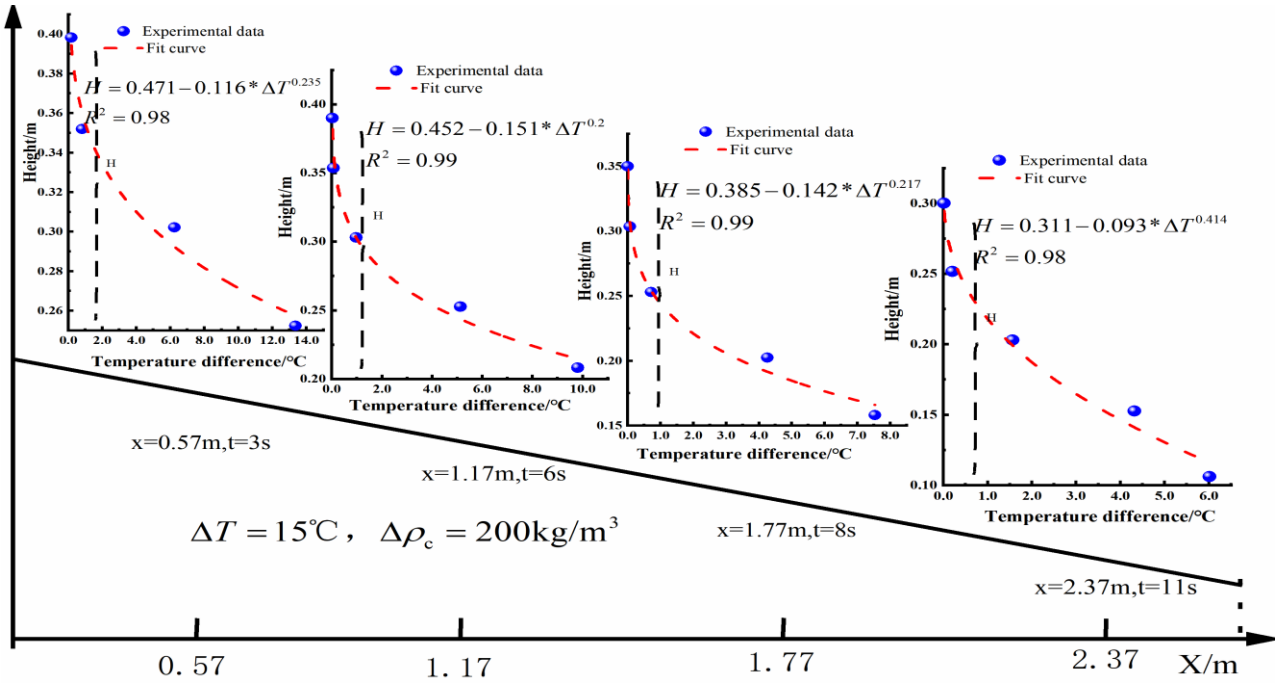

Figure A10. Maximum thermal shock temperature when passing through each group of sensors during turbidity migration (0–2.37 m) under experimental condition $\Delta T = 15$ °C, $\Delta\rho_c = 200$ kg/m^3.

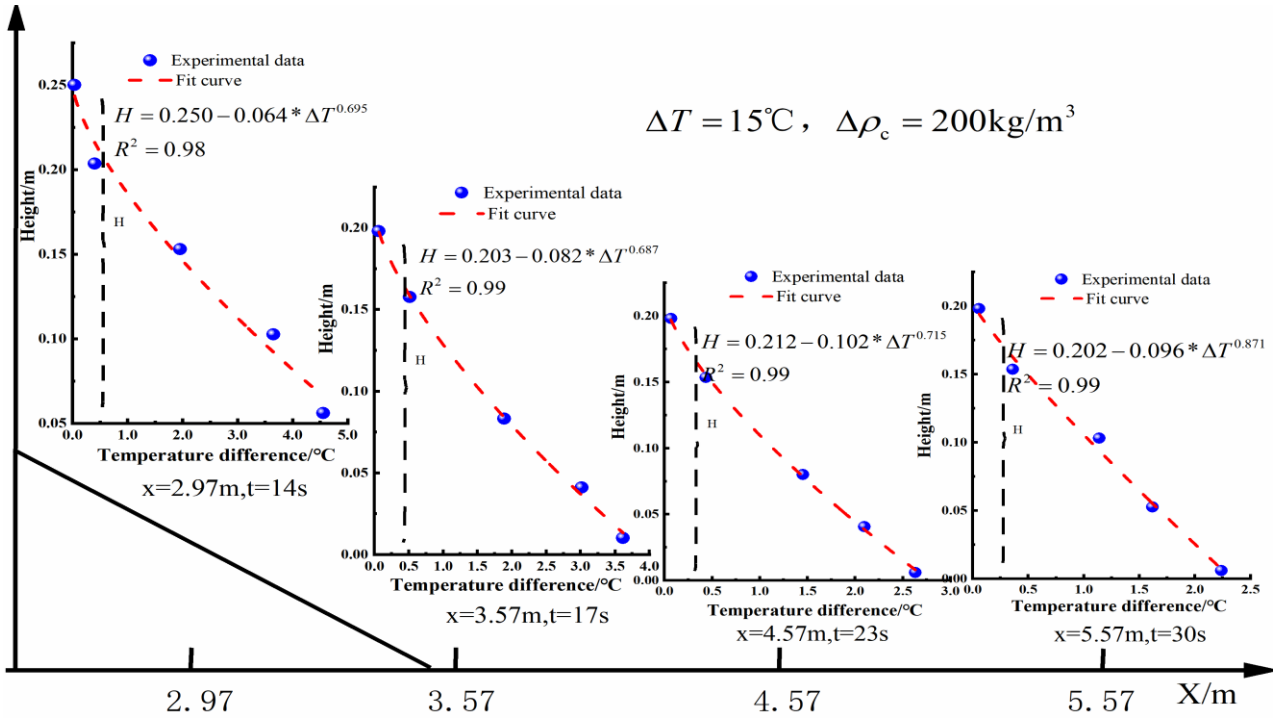

Figure A11. Maximum thermal shock temperature when passing through each group of sensors during turbidity migration (2.37–5.57 m) under experimental condition $\Delta T = 15$ °C, $\Delta\rho_c = 200$ kg/m^3.

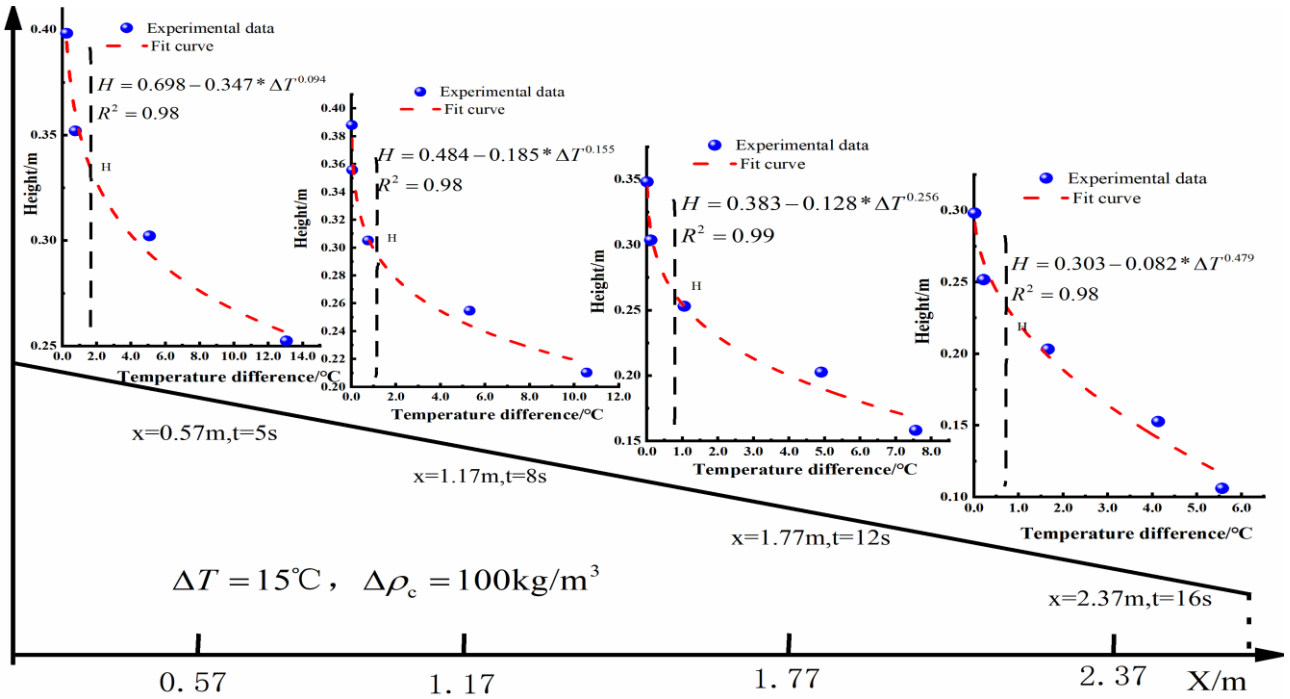

Figure A12. Maximum thermal shock temperature when passing through each group of sensors during turbidity migration (0–2.37 m) under experimental condition $\Delta T = 15$ °C, $\Delta\rho_c = 100$ kg/m^3.

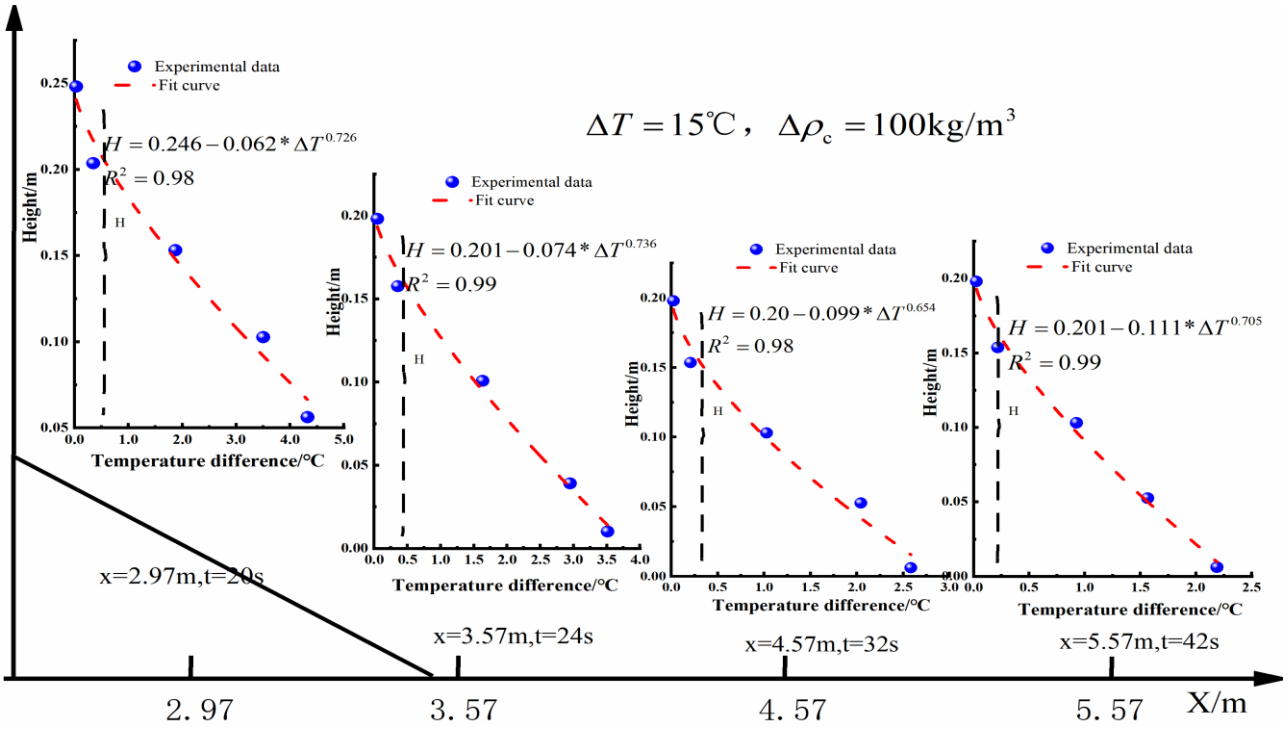

Figure A13. Maximum thermal shock temperature when passing through each group of sensors during turbidity migration (2.37–5.57 m) under experimental condition ΔT = 15 °C, $\Delta\rho_c$ = 100 kg/m^3.

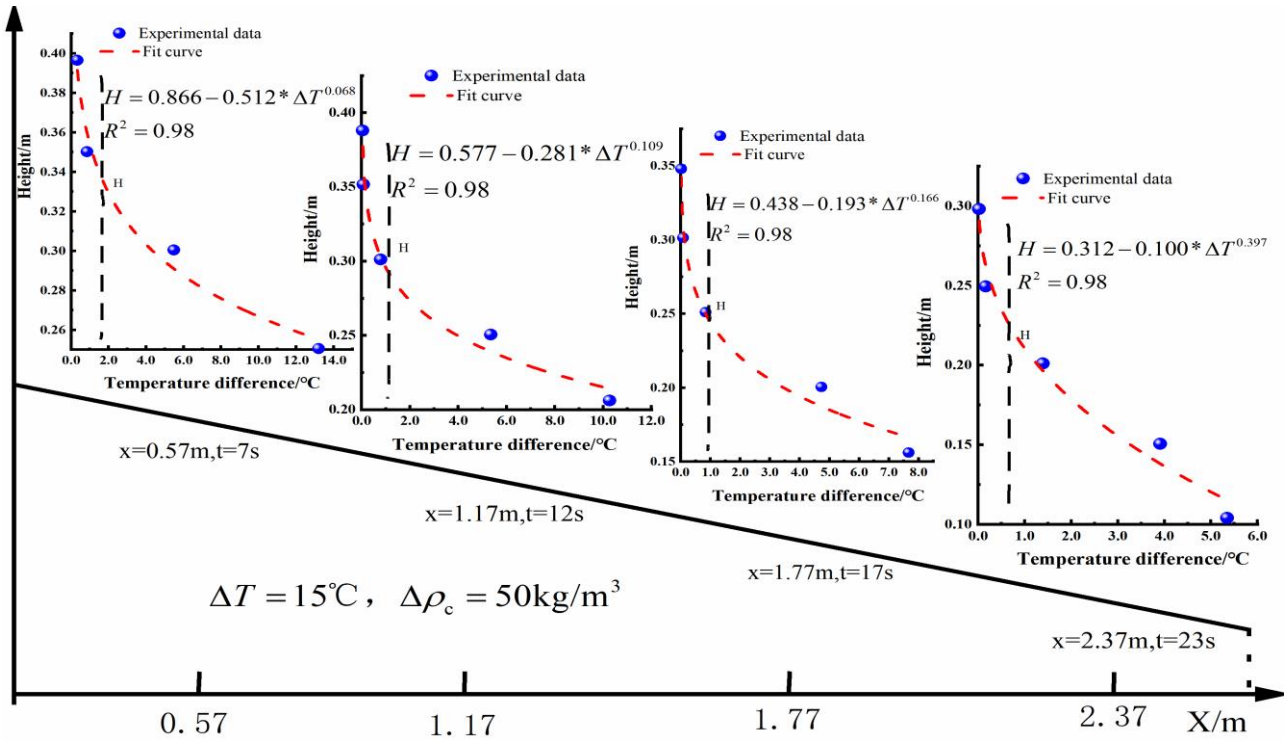

Figure A14. Maximum thermal shock temperature when passing through each group of sensors during turbidity migration (0–2.37 m) under experimental condition ΔT = 15 °C, $\Delta\rho_c$ = 50 kg/m^3.

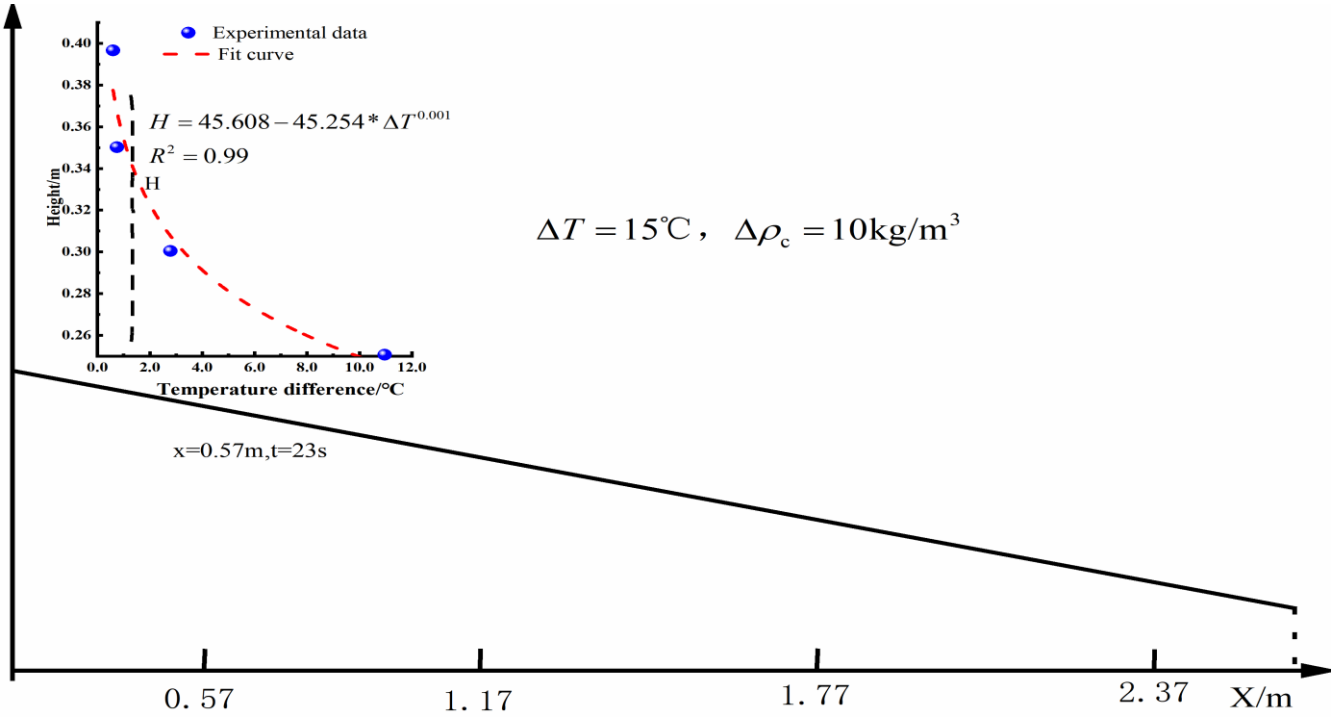

Figure A15. Maximum thermal shock temperature when passing through each group of sensors during turbidity migration (0–2.37 m) under experimental condition $\Delta T = 15$ °C, $\Delta\rho_c = 10$ kg/m^3.

References

1. Khripounoff, A.; Vangriesheim, A.; Babonneau, N.; Crassous, P.; Dennielou, B.; Savoye, B. Direct observation of intense turbidity current activity in the Zaire submarine valley at 4000 m water depth. *Mar. Geol.* **2003**, *194*, 151–158. [CrossRef]
2. Piper, D.J.; Normark, W.R. Processes that initiate turbidity currents and their influence on turbidites: A marine geology perspective. *J. Sediment. Res.* **2009**, *79*, 347–362. [CrossRef]
3. Talling, P.J.; Masson, D.G.; Sumner, E.J.; Malgesini, G. Subaqueous sediment density flows: Depositional processes and deposit types. *Sedim* **2012**, *59*, 1937–2003. [CrossRef]
4. Xu, J.; Noble, M.; Rosenfeld, L.K. In-situ measurements of velocity structure within turbidity currents. *GeoRL* **2004**, *31*. [CrossRef]
5. Tian, Z.; Huang, J.; Xiang, J.; Zhang, S. Suspension and transportation of sediments in submarine canyon induced by internal solitary waves. *PhFl* **2024**, *36*, 022112. [CrossRef]
6. Dalrymple, R.W.; Mackay, D.A.; Ichaso, A.A.; Choi, K.S. Processes, morphodynamics, and facies of tide-dominated estuaries. *Princ. Tidal Sedimentol.* **2012**, 79–107. [CrossRef]
7. Hage, S.; Galy, V.; Cartigny, M.; Acikalin, S.; Clare, M.; Gröcke, D.; Hilton, R.; Hunt, J.; Lintern, D.; McGhee, C. Efficient preservation of young terrestrial organic carbon in sandy turbidity-current deposits. *Geo* **2020**, *48*, 882–887. [CrossRef]
8. Kane, I.A.; Clare, M.A. Dispersion, accumulation, and the ultimate fate of microplastics in deep-marine environments: A review and future directions. *Front. Earth Sci.* **2019**, *7*, 80. [CrossRef]
9. Pohl, F.; Eggenhuisen, J.T.; Kane, I.A.; Clare, M.A. Transport and burial of microplastics in deep-marine sediments by turbidity currents. *Environ. Sci. Technol.* **2020**, *54*, 4180–4189. [CrossRef]
10. Tian, H.; Ren, Y.; Chen, Z.; Tao, W.; Wu, H.; Xu, G. Numerical Study of the Transport Process of Shallow Heat Carried by Turbidity Currents in Deep-Sea Environments. *J. Geophys. Res. Ocean.* **2023**, *128*, e2022JC019478. [CrossRef]
11. Danovaro, R.; Bianchelli, S.; Gambi, C.; Mea, M.; Zeppilli, D. α-, β-, γ-, δ-and ε-diversity of deep-sea nematodes in canyons and open slopes of Northeast Atlantic and Mediterranean margins. *Mar. Ecol. Prog. Ser.* **2009**, *396*, 197–209. [CrossRef]
12. Lambshead, P.J.D. *Marine Nematode Biodiversity*; Volume 1: Nematode morphology, physiology, and ecology; CABI Publishing: Wallingford, UK, 2004; pp. 438–468.
13. Heip, C.; Vincx, M.; Vranken, G. The ecology of marine nematodes. *Oceanogr. Mar. Biol.* **1985**, *23*, 399–489.
14. Danovaro, R.; Dell'Anno, A.; Pusceddu, A. Biodiversity response to climate change in a warm deep sea. *Ecol. Lett.* **2004**, *7*, 821–828. [CrossRef]
15. Paull, C.K.; Talling, P.J.; Maier, K.L.; Parsons, D.; Xu, J.; Caress, D.W.; Gwiazda, R.; Lundsten, E.M.; Anderson, K.; Barry, J.P. Powerful turbidity currents driven by dense basal layers. *Nat. Commun.* **2018**, *9*, 4114. [CrossRef]
16. Simmons, S.; Azpiroz-Zabala, M.; Cartigny, M.; Clare, M.; Cooper, C.; Parsons, D.; Pope, E.; Sumner, E.; Talling, P. Novel acoustic method provides first detailed measurements of sediment concentration structure within submarine turbidity currents. *J. Geophys. Res. Ocean.* **2020**, *125*, e2019JC015904. [CrossRef]

17. Hage, S.; Cartigny, M.J.; Sumner, E.J.; Clare, M.A.; Hughes Clarke, J.E.; Talling, P.J.; Lintern, D.G.; Simmons, S.M.; Silva Jacinto, R.; Vellinga, A.J. Direct monitoring reveals initiation of turbidity currents from extremely dilute river plumes. *Geophys. Res. Lett.* **2019**, *46*, 11310–11320. [CrossRef]
18. Kelly, R.; Dorrell, R.; Burns, A.; McCaffrey, W. The structure and entrainment characteristics of partially confined gravity currents. *J. Geophys. Res. Ocean.* **2019**, *124*, 2110–2125. [CrossRef]
19. Traer, M.; Hilley, G.; Fildani, A.; McHargue, T. The sensitivity of turbidity currents to mass and momentum exchanges between these underflows and their surroundings. *J. Geophys. Res. Earth Surf.* **2012**, *117*, 7. [CrossRef]
20. Gill, A.E. *Atmosphere-Ocean Dynamics*; Academic Press: Cambridge, MA, USA, 1982; Volume 30.
21. Hwang, J.-S.; Souissi, S.; Dahms, H.-U.; Tseng, L.-C.; Schmitt, F.G.; Chen, Q.-C. Rank-abundance allocations as a tool to analyze planktonic copepod assemblages off the Danshuei river estuary (Northern Taiwan). *Zool. Stud.* **2009**, *48*, 49–62.
22. Sparkes, R.B.; Lin, I.-T.; Hovius, N.; Galy, A.; Liu, J.T.; Xu, X.; Yang, R. Redistribution of multi-phase particulate organic carbon in a marine shelf and canyon system during an exceptional river flood: Effects of Typhoon Morakot on the Gaoping River–Canyon system. *Mar. Geol.* **2015**, *363*, 191–201. [CrossRef]
23. Wang, R.-M.; You, C.-F.; Chu, H.-Y.; Hung, J.-J. Seasonal variability of dissolved major and trace elements in the Gaoping (Kaoping) River Estuary, Southwestern Taiwan. *J. Mar. Syst.* **2009**, *76*, 444–456. [CrossRef]
24. Zhang, Y.; Liu, Z.; Zhao, Y.; Colin, C.; Zhang, X.; Wang, M.; Zhao, S.; Kneller, B.J.G. Long-term in situ observations on typhoon-triggered turbidity currents in the deep sea. *Geo* **2018**, *46*, 675–678. [CrossRef]
25. Puig, P.; Ogston, A.S.; Mullenbach, B.; Nittrouer, C.; Parsons, J.; Sternberg, R. Storm-induced sediment gravity flows at the head of the Eel submarine canyon, northern California margin. *J. Geophys. Res. Ocean.* **2004**, *109*, C03019. [CrossRef]
26. Xu, J.; Sequeiros, O.E.; Noble, M.A. Sediment concentrations, flow conditions, and downstream evolution of two turbidity currents, Monterey Canyon, USA. *Deep Sea Res. Part I* **2014**, *89*, 11–34. [CrossRef]
27. Bailey, L.P.; Clare, M.A.; Rosenberger, K.J.; Cartigny, M.J.; Talling, P.J.; Paull, C.K.; Gwiazda, R.; Parsons, D.R.; Simmons, S.M.; Xu, J. Preconditioning by sediment accumulation can produce powerful turbidity currents without major external triggers. *Earth Planet. Sci. Lett.* **2021**, *562*, 116845. [CrossRef]
28. Azpiroz-Zabala, M.; Cartigny, M.J.; Talling, P.J.; Parsons, D.R.; Sumner, E.J.; Clare, M.A.; Simmons, S.M.; Cooper, C.; Pope, E.L. Newly recognized turbidity current structure can explain prolonged flushing of submarine canyons. *Sci. Adv.* **2017**, *3*, e1700200. [CrossRef]
29. Descy, J.P.; Darchambeau, F.; Lambert, T.; Stoyneva-Gaertner, M.P.; Bouillon, S.; Borges, A.V. Phytoplankton dynamics in the Congo River. *Freshw. Biol.* **2017**, *62*, 87–101. [CrossRef]
30. Barats, A.; Féraud, G.; Potot, C.; Philippini, V.; Travi, Y.; Durrieu, G.; Dubar, M.; Simler, R. Naturally dissolved arsenic concentrations in the Alpine/Mediterranean Var River watershed (France). *Sci. Total Environ.* **2014**, *473*, 422–436. [CrossRef]
31. Khripounoff, A.; Crassous, P.; Bue, N.L.; Dennielou, B.; Jacinto, R.S. Different types of sediment gravity flows detected in the Var submarine canyon (northwestern Mediterranean Sea). *Prog. Oceanogr.* **2012**, *106*, 138–153. [CrossRef]
32. Palanques, A.; de Madron, X.D.; Puig, P.; Fabres, J.; Guillén, J.; Calafat, A.; Canals, M.; Heussner, S.; Bonnin, J. Suspended sediment fluxes and transport processes in the Gulf of Lions submarine canyons. The role of storms and dense water cascading. *Mar. Geol.* **2006**, *234*, 43–61. [CrossRef]
33. Halbwachs, M.; Sabroux, J.C.; Grangeon, J.; Kayser, G.; Tochon-Danguy, J.C.; Felix, A.; B'eard, J.C.; Villevieille, A.; Vitter, G.; Richon, P. Degassing the "killer lakes" Nyos and Monoun, Cameroon. *Eos Trans. Am. Geophys. Union* **2004**, *85*, 281–285. [CrossRef]
34. Sparks, R.S.J.; Bonnecaze, R.T.; Huppert, H.E.; Lister, J.R.; Hallworth, M.A.; Mader, H.; Phillips, J. Sediment-laden gravity currents with reversing buoyancy. *Earth Planet. Sci. Lett.* **1993**, *114*, 243–257. [CrossRef]
35. Cantelli, A.; Johnson, S.; White, J.; Parker, G. Sediment sorting in the deposits of turbidity currents created by experimental modeling of explosive subaqueous eruptions. *J. Geol.* **2008**, *116*, 76–93. [CrossRef]
36. Gladstone, C.; Pritchard, D. Patterns of deposition from experimental turbidity currents with reversing buoyancy. *Sedim* **2010**, *57*, 53–84. [CrossRef]
37. Hizzett, J.L.; Hughes Clarke, J.E.; Sumner, E.J.; Cartigny, M.; Talling, P.; Clare, M. Which triggers produce the most erosive, frequent, and longest runout turbidity currents on deltas? *GeoRL* **2018**, *45*, 855–863. [CrossRef]
38. Kineke, G.; Woolfe, K.; Kuehl, S.; Milliman, J.D.; Dellapenna, T.; Purdon, R. Sediment export from the Sepik River, Papua New Guinea: Evidence for a divergent sediment plume. *Cont. Shelf. Res.* **2000**, *20*, 2239–2266. [CrossRef]
39. Steel, E.; Buttles, J.; Simms, A.R.; Mohrig, D.; Meiburg, E. The role of buoyancy reversal in turbidite deposition and submarine fan geometry. *Geo* **2017**, *45*, 35–38. [CrossRef]
40. Steel, E.; Simms, A.R.; Warrick, J.; Yokoyama, Y. Highstand shelf fans: The role of buoyancy reversal in the deposition of a new type of shelf sand body. *Bulletin* **2016**, *128*, 1717–1724. [CrossRef]
41. Lu, G.; Wells, M.; van Strygen, I.; Hecky, R.E. Intrusions of sediment laden rivers into density stratified water columns could be an unrecognized source of mixing in many lakes and coastal oceans. *Sedim* **2022**, *69*, 2228–2245. [CrossRef]
42. Morton, B.; Taylor, G.I.; Turner, J.S. Turbulent gravitational convection from maintained and instantaneous sources. *Proc. R. Soc. Lond. Ser. A Math. Phys. Sci.* **1956**, *234*, 1–23. [CrossRef]
43. Jacobson, M.; Testik, F.Y. Turbulent entrainment into fluid mud gravity currents. *Environ. Fluid Mech.* **2014**, *14*, 541–563. [CrossRef]
44. Han, D.; He, Z.; Lin, Y.T.; Wang, Y.; Guo, Y.; Yuan, Y. Hydrodynamics and sediment transport of downslope turbidity current through rigid vegetation. *Water Resour. Res.* **2023**, *59*, e2023WR034421. [CrossRef]

45. He, Z.; Zhao, L.; Lin, T.; Hu, P.; lv, Y.; Ho, H.-C.; Lin, Y.-T. Hydrodynamics of gravity currents down a ramp in linearly stratified environments. *J. Hydraul. Eng.* **2017**, *143*, 04016085. [CrossRef]
46. Carter, L.; Gavey, R.; Talling, P.J.; Liu, J.T. Insights into submarine geohazards from breaks in subsea telecommunication cables. *Oceanography* **2014**, *27*, 58–67. [CrossRef]
47. Talling, P.J.; Clare, M.L.; Urlaub, M.; Pope, E.; Hunt, J.E.; Watt, S.F. Large submarine landslides on continental slopes: Geohazards, methane release, and climate change. *Oceanography* **2014**, *27*, 32–45. [CrossRef]
48. Tanaka, M.; Girard, G.; Davis, R.; Peuto, A.; Bignell, N. Recommended table for the density of water between 0 C and 40 C based on recent experimental reports. *Metro* **2001**, *38*, 301. [CrossRef]
49. Kneller, B.; Nasr-Azadani, M.M.; Radhakrishnan, S.; Meiburg, E. Long-range sediment transport in the world's oceans by stably stratified turbidity currents. *J. Geophys. Res. Ocean.* **2016**, *121*, 8608–8620. [CrossRef]
50. Giorgio Serchi, F.; Peakall, J.; Ingham, D.; Burns, A. A unifying computational fluid dynamics investigation on the river-like to river-reversed secondary circulation in submarine channel bends. *J. Geophys. Res. Ocean.* **2011**, *116*. [CrossRef]
51. Sequeiros, O.E.; Spinewine, B.; Beaubouef, R.T.; Sun, T.; García, M.H.; Parker, G. Characteristics of velocity and excess density profiles of saline underflows and turbidity currents flowing over a mobile bed. *J. Hydraul. Eng.* **2010**, *136*, 412–433. [CrossRef]
52. Hiscott, R.N. Loss of capacity, not competence, as the fundamental process governing deposition from turbidity currents. *J. Sediment. Res.* **1994**, *64*, 209–214. [CrossRef]
53. Sumner, E.J.; Amy, L.A.; Talling, P.J. Deposit structure and processes of sand deposition from decelerating sediment suspensions. *J. Sediment. Res.* **2008**, *78*, 529–547. [CrossRef]
54. Johnson, H.P.; Miller, U.K.; Salmi, M.S.; Solomon, E.A. Analysis of bubble plume distributions to evaluate methane hydrate decomposition on the continental slope. *Geochem. Geophys. Geosyst.* **2015**, *16*, 3825–3839. [CrossRef]
55. Phrampus, B.J.; Hornbach, M.J. Recent changes to the Gulf Stream causing widespread gas hydrate destabilization. *Nature* **2012**, *490*, 527–530. [CrossRef]
56. Dorrell, R.; Peakall, J.; Sumner, E.; Parsons, D.; Darby, S.; Wynn, R.; Özsoy, E.; Tezcan, D. Flow dynamics and mixing processes in hydraulic jump arrays: Implications for channel-lobe transition zones. *Mar. Geol.* **2016**, *381*, 181–193. [CrossRef]
57. Meiburg, E.; Kneller, B. Turbidity currents and their deposits. *AnRFM* **2010**, *42*, 135–156. [CrossRef]
58. Turner, J. Turbulent entrainment: The development of the entrainment assumption, and its application to geophysical flows. *JFM* **1986**, *173*, 431–471. [CrossRef]
59. Imran, J.; Khan, S.M.; Pirmez, C.; Parker, G. Froude scaling limitations in modeling of turbidity currents. *Environ. Fluid Mech.* **2017**, *17*, 159–186. [CrossRef]
60. Akan, A.O.; Iyer, S.S. *Open Channel Hydraulics*; Butterworth-Heinemann: Oxford, UK, 2021.
61. Task Committee on Hydraulic Modeling of the Environmental; Water Resources Institute of ASCE. *Hydraulic Modeling: Concepts and Practice*; ACSE: Reston, VA, USA, 2000.
62. Marino, M.; Stagnitti, M.; Stancanelli, L.M.; Musumeci, R.E.; Foti, E. Dynamics of wave-supported gravity currents in intermediate water. *Cont. Shelf. Res.* **2023**, *267*, 105082. [CrossRef]
63. Monaghan, J. Gravity currents and solitary waves. *Phys. D Nonlinear Phenom.* **1996**, *98*, 523–533. [CrossRef]
64. Tian, Z.; Liu, C.; Jia, Y.; Song, L.; Zhang, M. Submarine trenches and wave-wave interactions enhance the sediment resuspension induced by internal solitary waves. *J. Ocean Univ. China* **2023**, *22*, 983–992. [CrossRef]
65. Falcini, F.; Fagherazzi, S.; Jerolmack, D. Wave-supported sediment gravity flows currents: Effects of fluid-induced pressure gradients and flow width spreading. *Cont. Shelf. Res.* **2012**, *33*, 37–50. [CrossRef]
66. Tian, Z.; Huang, J.; Xiang, J.; Zhang, S.; Wu, J.; Liu, X.; Luo, T.; Yue, J. Interaction between internal solitary waves and the seafloor in the deep sea. *Deep. Undergr. Sci. Eng.* **2024**, *3*, 149–162. [CrossRef]
67. Piper, D.J.; Cochonat, P.; Morrison, M.L. The sequence of events around the epicentre of the 1929 Grand Banks earthquake: Initiation of debris flows and turbidity current inferred from sidescan sonar. *Sedim* **1999**, *46*, 79–97. [CrossRef]
68. Rothwell, R.; Thomson, J.; Kähler, G. Low-sea-level emplacement of a very large Late Pleistocene 'megaturbidite'in the western Mediterranean Sea. *Nature* **1998**, *392*, 377–380. [CrossRef]
69. Talling, P.; Wynn, R.; Masson, D.; Frenz, M.; Cronin, B.; Schiebel, R.; Akhmetzhanov, A.; Dallmeier-Tiessen, S.; Benetti, S.; Weaver, P. Onset of submarine debris flow deposition far from original giant landslide. *Nature* **2007**, *450*, 541–544. [CrossRef]
70. Milliman, J.D.; Syvitski, J.P. Geomorphic/tectonic control of sediment discharge to the ocean: The importance of small mountainous rivers. *J. Geol.* **1992**, *100*, 525–544. [CrossRef]
71. Kao, S.; Dai, M.; Selvaraj, K.; Zhai, W.; Cai, P.; Chen, S.; Yang, J.; Liu, J.; Liu, C.; Syvitski, J. Cyclone-driven deep sea injection of freshwater and heat by hyperpycnal flow in the subtropics. *Geophys. Res. Lett.* **2010**, *37*, L21702. [CrossRef]